Astronomy & Astrophysics manuscript no. DL07˙Planck˙v20
February 13, 2015

Planck intermediate results. XXIX. All-sky dust modelling with *Planck*, *IRAS*, and *WISE* observations

Planck Collaboration: P. A. R. Ade[78], N. Aghanim[54], M. I. R. Alves[54], G. Aniano[54], M. Arnaud[66], M. Ashdown[63,5], J. Aumont[54], C. Baccigalupi[77], A. J. Banday[84,9], R. B. Barreiro[60], N. Bartolo[27], E. Battaner[86,87], K. Benabed[55,83], A. Benoit-Lévy[21,55,83], J.-P. Bernard[84,9], M. Bersanelli[30,46], P. Bielewicz[84,9,77], A. Bonaldi[62], L. Bonavera[60], J. R. Bond[8], J. Borrill[12,80], F. R. Bouchet[55,83], F. Boulanger[54], C. Burigana[45,28,47], R. C. Butler[45], E. Calabrese[82], J.-F. Cardoso[67,1,55], A. Catalano[68,65], A. Chamballu[66,14,54], H. C. Chiang[24,6], P. R. Christensen[74,33], D. L. Clements[51], S. Colombi[55,83], L. P. L. Colombo[20,61], F. Couchot[64], B. P. Crill[61,75], A. Curto[5,60], F. Cuttaia[45], L. Danese[77], R. D. Davies[62], R. J. Davis[62], P. de Bernardis[29], A. de Rosa[45], G. de Zotti[42,77], J. Delabrouille[1], C. Dickinson[62], J. M. Diego[60], H. Dole[54,53], S. Donzelli[46], O. Doré[61,10], M. Douspis[54], B. T. Draine[76], A. Ducout[55,51], X. Dupac[36], G. Efstathiou[57], F. Elsner[55,83], T. A. Enßlin[71], H. K. Eriksen[58], E. Falgarone[65], F. Finelli[45,47], O. Forni[84,9], M. Frailis[44], A. A. Fraisse[24], E. Franceschi[45], A. Frejsel[74], S. Galeotta[44], S. Galli[55], K. Ganga[1], T. Ghosh[54], M. Giard[84,9], E. Gjerløw[58], J. González-Nuevo[60,77], K. M. Górski[61,88], A. Gregorio[31,44,49], A. Gruppuso[45], V. Guillet[54], F. K. Hansen[58], D. Hanson[72,61,8], D. L. Harrison[57,63], S. Henrot-Versillé[64], C. Hernández-Monteagudo[11,71], D. Herranz[60], S. R. Hildebrandt[61], E. Hivon[55,83], M. Hobson[5], W. A. Holmes[61], W. Hovest[71], K. M. Huffenberger[22], G. Hurier[54], A. H. Jaffe[51], T. R. Jaffe[84,9], W. C. Jones[24], M. Juvela[23], E. Keihänen[23], R. Keskitalo[12], T. S. Kisner[70], R. Kneissl[35,7], J. Knoche[71], M. Kunz[16,54,2], H. Kurki-Suonio[23,40], G. Lagache[54], J.-M. Lamarre[65], A. Lasenby[5,63], M. Lattanzi[28], C. R. Lawrence[61], R. Leonardi[36], F. Levrier[65], M. Liguori[27], P. B. Lilje[58], M. Linden-Vørnle[15], M. López-Caniego[60], P. M. Lubin[25], J. F. Macías-Pérez[68], B. Maffei[62], D. Maino[30,46], N. Mandolesi[45,4,28], M. Maris[44], D. J. Marshall[66], P. G. Martin[8], E. Martínez-González[60], S. Masi[29], S. Matarrese[27], P. Mazzotta[32], A. Melchiorri[29,48], L. Mendes[36], A. Mennella[30,46], M. Migliaccio[57,63], M.-A. Miville-Deschênes[54,8], A. Moneti[55], L. Montier[84,9], G. Morgante[45], D. Mortlock[51], D. Munshi[78], J. A. Murphy[73], P. Naselsky[74,33], P. Natoli[28,3,45], H. U. Nørgaard-Nielsen[15], D. Novikov[51], I. Novikov[74], C. A. Oxborrow[15], L. Pagano[29,48], F. Pajot[54], R. Paladini[52], D. Paoletti[45,47], F. Pasian[44], O. Perdereau[64], L. Perotto[68], F. Perrotta[77], V. Pettorino[39], F. Piacentini[29], M. Piat[1], S. Plaszczynski[64], E. Pointecouteau[84,9], G. Polenta[3,43], N. Ponthieu[54,50], L. Popa[56], G. W. Pratt[66], S. Prunet[55,83], J.-L. Puget[54], J. P. Rachen[18,71], W. T. Reach[85], R. Rebolo[59,13,34], M. Reinecke[71], M. Remazeilles[62,54,1], C. Renault[68], I. Ristorcelli[84,9], G. Rocha[61,10], G. Roudier[1,65,61], J. A. Rubiño-Martín[59,34], B. Rusholme[52], M. Sandri[45], D. Santos[68], D. Scott[19], L. D. Spencer[78], V. Stolyarov[5,63,81], R. Sudiwala[78], R. Sunyaev[71,79], D. Sutton[57,63], A.-S. Suur-Uski[23,40], J.-F. Sygnet[55], J. A. Tauber[37], L. Terenzi[38,45], L. Toffolatti[17,60,45], M. Tomasi[30,46], M. Tristram[64], M. Tucci[16,64], G. Umana[41], L. Valenziano[45], J. Valiviita[23,40], B. Van Tent[69], P. Vielva[60], F. Villa[45], L. A. Wade[61], B. D. Wandelt[55,83,26], I. K. Wehus[61], N. Ysard[23], D. Yvon[14], A. Zacchei[44], and A. Zonca[25]

(Affiliations can be found after the references)

Preprint online version: February 13, 2015

ABSTRACT

We present all-sky dust modelling of the high resolution *Planck*, *IRAS* and *WISE* infrared (IR) observations using the physical dust model presented by Draine & Li in 2007 (DL). We study the performance of this model and present implications for future dust modelling. The present work extends to the full sky the dust modelling carried out on nearby galaxies using *Herschel* and *Spitzer* data. We employ the DL dust model to generate maps of the dust mass surface density Σ_{M_d}, the dust optical extinction A_V, and the starlight intensity heating the bulk of the dust, parametrized by $U_{\rm min}$. We test the model by comparing these maps with independent estimates of the dust optical extinction A_V. The DL model reproduces the observed spectral energy distribution (SED) satisfactorily over most of the sky, with small deviations in the inner Galactic disk, and in low ecliptic latitude areas, presumably due to zodiacal light contamination. In the Andromeda galaxy (M31), the present dust mass estimates agree remarkably well (within 10 %) with DL estimates based on independent *Spitzer* and *Herschel* data. In molecular clouds, we compare the DL A_V estimates with maps generated from stellar optical observations from the 2MASS survey. The DL A_V estimates are a factor of about 3 larger than values estimated from 2MASS observations. In the diffuse interstellar medium (ISM) we compare the DL optical extinction A_V estimates with optical estimates from approximately 2×10^5 quasi-stellar objects (QSOs) observed in the Sloan digital sky survey. The DL A_V estimates are larger than those determined from the QSOs, and this discrepancy depends on $U_{\rm min}$. We propose an empirical renormalization of the DL A_V estimate, dependent of $U_{\rm min}$, which compensates for the systematic differences found here. This renormalization, bringing into agreement the A_V estimates on QSOs, also brings into agreement the A_V estimates on molecular clouds. In the diffuse ISM, the DL fitting parameter $U_{\rm min}$, effectively determined by the wavelength where the SED peaks, appears to trace variations in the far-IR opacity of the dust grains. Therefore, some of the physical assumptions of the DL model need to be revised. We provide a family of SEDs normalized by optical reddening, parameterized by $U_{\rm min}$; these will be the constraints for a next generation of dust models.

Key words. ISM: general – Galaxy: general – submillimeter: ISM

1. Introduction

Studying the interstellar medium (ISM) is important in a wide range of astronomical disciplines, from star and planet formation to galaxy evolution. Dust changes the appearance of galaxies by absorbing ultraviolet (UV), optical, and infrared (IR) starlight, and emitting mid-IR and far-IR (FIR) radiation. Dust is an important agent in the chemical and thermodynamical evolution of the ISM. Physical models of interstellar dust that have been developed are constrained by such observations. In the present work, we study the ability of a physical dust model to reproduce

IR emission and optical extinction observations, using the newly available *Planck*[1] data.

The *Planck* data provide a full-sky view of the Milky Way (MW) at submillimetre (submm) wavelengths, with much higher angular resolution than earlier maps made by the Diffuse Infrared Background Experiment (DIRBE) (Silverberg et al. 1993) on the *Cosmic background explorer* (*COBE*) spacecraft (Boggess et al. 1992). These new constraints on the spectral energy distribution (SED) emission of large dust grains were modelled by Planck Collaboration XI (2014, hereafter *Pl*-MBB) using a modified blackbody (MBB) spectral model, parameterized by optical depth and dust temperature. That study, along with previous *Planck* results, confirmed spatial changes in the dust submm opacity even in the high latitude sky (Planck Collaboration XXIV 2011; Planck Collaboration Int. XVII 2014). The dust temperature, which reflects the thermal equilibrium, is anti-correlated with the FIR opacity. The dust temperature is also affected by the strength of the interstellar radiation field (ISRF) heating the dust. The bolometric emission per H atom is rather constant at high latitude, consistent with a uniform ISRF, but over the full sky, covering lines of sight through the Galaxy, the ISRF certainly changes. The all-sky submm dust optical depth was also calibrated in terms of optical extinction. However, no attempt was made to connect these data with a self-consistent dust model. That is the goal of this complementary paper.

Several authors have modelled the dust absorption and emission in the diffuse ISM, e.g. Draine & Lee (1984); Desert et al. (1990); Dwek (1998); Zubko et al. (2004); Compiègne et al. (2011); Jones et al. (2013); Siebenmorgen et al. (2014). We focus on one of the most widely used dust models presented by Draine & Li (2007, hereafter DL). Earlier, Draine & Lee (1984) studied the optical properties of graphite and silicate dust grains, while Weingartner & Draine (2001) and Li & Draine (2001) developed a carbonaceous-silicate grain model that has been quite successful in reproducing observed interstellar extinction, scattering, and IR emission. DL presented an updated physical dust model, extensively used to model starlight absorption and IR emission. The DL dust model employs a mixture of amorphous silicate grains and carbonaceous grains. The grains are assumed to be heated by a distribution of starlight intensities. The model assumes optical properties of the dust grains and the model SEDs are computed from first principles.

The DL model has been successfully employed to study the ISM in a variety of galaxies. Draine et al. (2007) employed DL to estimate the dust masses, abundances of polycyclic aromatic hydrocarbon (PAH) molecules, and starlight intensities in the *Spitzer* Infrared Nearby Galaxies Survey – Physics of the Star-Forming ISM and Galaxy Evolution (SINGS, Kennicutt et al. 2003) galaxy sample. This survey observed a sample of 75 nearby (within 30 Mpc of the Galaxy) galaxies, covering the full range in a 3-dimensional parameter space of physical properties, with the *Spitzer Space Telescope* (Werner et al. 2004). Wiebe et al. (2009) used the DL model with Balloon-borne Large Aperture Submillimeter Telescope (BLAST, Pascale et al. 2008) and *Spitzer* data to fit SEDs for seven nearby galaxies, finding a normalization discrepancy with the dust emission from MBB fits. The Key Insights on Nearby Galaxies: a FIR Survey with *Herschel* (KINGFISH) project, additionally observed a subsample of 61 of the SINGS galaxies with the *Herschel Space Observatory* (Pilbratt et al. 2010). Aniano et al. (2012) presented a detailed resolved study of two KINGFISH galaxies, NGC 628 and NGC 6946, using the DL model constrained by *Spitzer* and *Herschel* photometry. Aniano et al. (2014) extended the preceding study to the full KINGFISH sample of galaxies. Draine et al. (2014, hereafter DA14), presented a resolved study of the nearby Andromeda galaxy (M31), where high spatial resolution can be achieved. The DL model proved able to reproduce the observed emission from dust in the KINGFISH galaxies and M31. Ciesla et al. (2014) used the DL model to fit the volume limited, K-band selected sample of galaxies of the *Herschel* Reference Survey (Boselli et al. 2010), finding it systematically underestimated the 500 μm photometry.

The new *Planck* all-sky maps, combined with ancillary *Infrared Astronomical Satellite* (*IRAS*, Neugebauer et al. 1984) and *Wide-field Infrared Survey Explorer* (*WISE*, Wright et al. 2010) maps allow us to explore the dust thermal emission from the MW ISM with greater spatial resolution and frequency coverage than ever before. Here we test the compatibility of the DL dust model with these new observations.

We employ *WISE* 12[2] (12 μm), *IRAS* 60 (60 μm), *IRAS* 100 (100 μm), *Planck* 857 (350 μm), *Planck* 545 (550 μm), and *Planck* 353 (850 μm) maps to constrain the dust emission SED in the range 10 μm $< \lambda <$ 970 μm. These data allow us to generate reliable maps of the dust emission using a Gaussian point spread function (PSF) with 5′ full width at half maximum (FWHM). Working at lower resolution (1° FWHM), we can add the DIRBE 140 and DIRBE 240 photometric constraints.

We employ the DL dust model to characterize:

- the dust mass surface density Σ_{M_d};
- the dust optical extinction A_V;
- the dust mass fraction in small PAH grains q_PAH;
- the fraction of the total luminosity radiated by dust that arises from dust heated by intense radiation fields, f_PDR;
- the starlight intensity U_min heating the bulk of the dust.

The estimated dust parameters for M31 are compared with those derived using the independent maps in DA14.

We compare the DL optical extinction estimates with those of *Pl*-MBB. We further compare the DL model reddening estimates with near IR reddening estimates from quasi-stellar objects (QSOs) and from stellar reddening maps in dark clouds obtained from 2MASS (Skrutskie et al. 2006). These reveal significant systematic discrepancies that will require a revision of the DL model. We find an empirical parameterization that renormalizes the current DL model and provides insight into what is being compensated for through the renormalization.

We determine the observed FIR intensity per unit of optical extinction that should be reproduced by the next generation of self-consistent dust models. We also provide the *Planck* 217 (1.38 mm) and *Planck* 143 (2.10 mm) photometric constraints, which are not used in the current dust modelling.

This paper is organized as follows. In Section 2 we describe the data sets used. In Section 3 we present the DL dust model:

[1] *Planck* (`http://www.esa.int/Planck`) is a project of the European Space Agency (ESA) with instruments provided by two scientific consortia funded by ESA member states (in particular the lead countries France and Italy), with contributions from NASA (USA) and telescope reflectors provided by a collaboration between ESA and a scientific consortium led and funded by Denmark.

[2] From now on we will refer to the *WISE*, *IRAS*, and DIRBE bands as *WISE* 12, *IRAS* 60, *IRAS* 100, DIRBE 100, DIRBE 140, and DIRBE 240, by attaching the band reference wavelength (in μm) to the spacecraft or instrument name, and to the *Planck* bands as *Planck* 857, *Planck* 545, *Planck* 353, *Planck* 217, *Planck* 143, and *Planck* 100, by attaching the band reference frequency (in GHz) to the spacecraft name.

in Section 3.1 the model parametrization; and in Section 3.2 the model-fitting strategy. In Section 4 we describe the modelling results, robustness, and validation: we present the model parameter maps (Section 4.1); we analyze the model ability to fit the data (Sect. 4.2); the importance of *IRAS* 60 as a constraint (Sect. 4.3.1); and the dependence of the mass estimate on the data sets (Sect. 4.3.2). In Section 4.4 we compare the dust Σ_{M_d} estimates for M31 with independent estimates based on different data sets. In Section 5 we compare the dust A_V estimates with the MBB all-sky modelling results from *Pl*-MBB. In Section 6 we compare the dust A_V estimates on diffuse regions with estimates from QSO colours. In Section 6.3 we propose a dust model empirical correction (called "renormalization") to compensate for the discrepancies found. In Section 6.4 we present the observed FIR intensity per unit of optical extinction, i.e., the new photometric constraints that should be fitted by the next generation of dust models. In Section 7 we compare the dust A_V predictions with estimates from stellar observations toward molecular clouds and the performance of the renormalized model in these environments. In Section 8 we discuss the discrepancy of the FIR emission per unit of optical extinction of the DL model. We conclude in Section 9. In Appendix A we show the details of the comparison on M31 presented in Section 4.4. In Appendix B we present the details of the QSO A_V estimation. In Appendix C we analyze the impact of cosmic infrared background (CIB) anisotropies in our dust modelling.

2. Data sets

We use the publicly available, nominal mission *Planck* maps (Planck Collaboration I 2014). The zodiacal light has been estimated and removed (Planck Collaboration XIV 2014) from these maps. The cosmic microwave background, provided by the `SMICA` algorithm (Planck Collaboration XII 2014), was also removed from each *Planck* map. We use the zero level estimation and unit conversion factors given in *Pl*-MBB. A residual dipole oriented toward $l = 263\overset{\circ}{.}99$, $b = 48\overset{\circ}{.}26$, and a constant offset were removed from the maps to adjust them to a coherent Galactic zero level (*Pl*-MBB). We have checked that the results of this manuscript are not significantly changed when we use the most recent version of the *Planck* data available within the *Planck* consortium.

We additionally use *IRAS* 60 and *IRAS* 100 maps. We employ the *IRAS* 100 map presented in *Pl*-MBB. It combines the small scale ($< 30'$) features of the map presented by the improved reprocessing of the *IRAS* survey (IRIS) team by Miville-Deschênes & Lagache (2005), and the large scale ($> 30'$) features of the map presented by Schlegel et al. (1998, hereafter SFD). The zodiacal light emission has been estimated and removed from the SFD map, and therefore it is removed from the map we are employing[3]. We employ the *IRAS* 60 map presented by the IRIS team, with a custom estimation and removal of the zodiacal light[4].

WISE mapped the sky at 3.4, 4.6, 12, and 22 μm. Meisner & Finkbeiner (2014) presented a reprocessing of the entire *WISE* 12 imaging data set, generating a high resolution, full-sky map that is free of compact sources and was cleaned from several contaminating artefacts. The zodiacal light contribution was estimated and subtracted using the model presented by Kelsall et al. (1998). About 18 % of the sky is still contaminated by the Moon or other solar system objects. Aniano et. al, (A14, in preparation) presents an improved data reduction and artefact removal for the *WISE* 12 data, which we use in the present modelling. The zodiacal light contamination has been removed more effectively from *WISE* 12 than from its *IRAS* counterpart, and therefore we do not include *IRAS* 12 or *IRAS* 25. Currently, there is no artefact-free *WISE* 22 full-sky map available.

For typical lines of sight in the diffuse ISM, the dust SED peaks in the $\lambda = 100 - 160$ μm range. Unfortunately, no high resolution, all-sky maps are available in this wavelength range[5]. DIRBE produced low resolution (FWHM $= 42'$) all-sky maps at 140 and 240 μm, which can be used to test the robustness of our modelling. Additionally, we perform a lower resolution (1° FWHM) modelling, including the DIRBE 140 and DIRBE 240 photometric constraints. We use the DIRBE zodiacal light-subtracted mission average (ZSMA) maps. This modelling allows us to evaluate the importance of adding photometric constraints near the dust SED peak, which are absent in the *Planck* and *IRAS* data.

The most relevant information on the data sets that are used is presented in Table 1. The amplitudes of the CIB anisoropies (CIBA), which depend on the angular scale used, are listed in Table 1 correspond to those at the modelling resolution. Following *Pl*-MBB we do not remove the CO contributions to the *Planck* bands[6].

All maps were convolved to yield a Gaussian PSF, with FWHM $= 5\overset{'}{.}0$, slightly broader than all the maps' native resolution. Small residual zodiacal light is still present in the maps, potentially affecting the dust mass estimates in low ecliptic latitude areas. We use the Hierarchical Equal Area isoLatitude Pixelization (`HEALPix`) of a sphere coordinates (Górski et al. 2005)[7]. We work at resolution $N_{\rm side} = 2048$, so the maps have a total of $12 \times 2048 \times 2048 = 50331648$ pixels. Each pixel is a quadrilateral of area 2.94 arcmin^2 (i.e., about $1\overset{'}{.}7$ on a side). All maps and results presented in the current paper are performed using this resolution, except those of Sects.4.3.2 and 6.4.

3. The DL model

The DL dust model is a physical approach to modelling dust. It assumes that the dust consists of a mixture of amorphous silicate grains and carbonaceous grains heated by a distribution of starlight intensities. We employ the "Milky Way" grain size distributions (Weingartner & Draine 2001), chosen to reproduce the wavelength dependence of the average interstellar extinction within a few kiloparsec of the Sun. The silicate and carbonaceous content of the dust grains has been constrained by observations of the gas phase depletions in the ISM. The carbonaceous grains are assumed to have the properties of PAH molecules or clusters when the number of carbon atoms per grain $N_{\rm C} \lesssim 10^5$, but to have the properties of graphite when $N_{\rm C} \gg 10^5$. DL de-

[3] The zodiacal light emission contributes mainly at scales larger than $30'$, therefore, its contribution is subtracted when we retain the large scales of the SDF map.

[4] The new IRIS data reduction and a description are available at `http://www.cita.utoronto.ca/~mamd/IRIS/IrisOverview.html`

[5] The FIS instrument (Kawada et al. 2007) on board the *Akari* spacecraft (Murakami et al. 2007) observed the sky at four FIR bands in the 50 – 180 μm range, but the data are not yet public.

[6] The current CO maps are noisy in the low surface brightness areas, and therefore subtracting these small contributions increases the noise level significantly.

[7] A full description of `HEALPix` and its software library can be found at `http://healpix.jpl.nasa.gov`.

Table 1. Description of the data used.

Band	λ[a]	FWHM[b]	Calibration Uncertainty[c]	Offset[d]	Dipole[e]	CIB anisotropies[f]
	[μm]	[arcmin]	[%]	[MJy sr^{-1}]	[MJy sr^{-1}]	[MJy sr^{-1}]
Planck 100 GHz[g]	3000	9.66	0.5	0.00403 ± 0.00078	−0.0023821 ± 0.0000075	
Planck 143 GHz[g]	2098	7.27	0.5	0.01324 ± 0.00092	−0.0034858 ± 0.0000081	
Planck 217 GHz[g]	1283	5.01	0.5	0.0384 ± 0.0029	−0.006067 ± 0.000017	
Planck 353 GHz	850	4.86	1.2	0.085 ± 0.011	−0.008939 ± 0.000043	0.019
Planck 545 GHz	550	4.84	10.0	0.095 ± 0.036	0.014806 ± 0.000091	0.059
Planck 857 GHz	350	4.63	10.0	0.09 ± 0.10	0 ± 0	0.010
DIRBE 240 μm	248	42.0	11.6	0.8499 ± 0.0085		
DIRBE 140 μm	148	42.0	10.6	0.9088 ± 0.0147		
DIRBE 100 μm	100	42.0	13.6	0.5841 ± 0.0050		
IRAS 100 μm	100	4.3	13.5	−0.1743 ± 0.0050		0.090
IRAS 60 μm	60	4.0	10.4	0.3442 ± 0.0014		0.048
WISE 12 μm	12	0.25	10.0			

a Mean band wavelength.
b FWHM of the PSF of the original map.
c Assumed calibration uncertainty as a percentage of the image intensity.
d Zero level subtracted from the map.
e Residual dipole oriented towards $l = 263.^{\circ}99$, $b = 48.^{\circ}26$, subtracted from the map.
f Root mean square (rms) of the CIB anisotropies in the band at 5′ resolution.
g *Planck* 217, *Planck* 143, and *Planck* 100 bands are not used to constraint the current dust model.

scribes the detailed computation of the model SED, and AD12 describes its use in modelling resolved dust emission regims.

3.1. Parameterization

The IR emission of the DL dust model is parametrized by six parameters, Σ_{M_d}, $q_{\rm PAH}$, $U_{\rm min}$, $U_{\rm max}$, α, and γ. The definition of these parameters is now reviewed.

The model IR emission is proportional to the dust mass surface density Σ_{M_d}.

The PAH abundance is measured by the parameter $q_{\rm PAH}$, defined to be the fraction of the total grain mass contributed by PAHs containing $N_{\rm C} < 10^3$ C atoms[8]. As a result of single-photon heating, the tiny PAHs contributing to $q_{\rm PAH}$ radiate primarily at $\lambda < 30\,\mu$m, and this fraction is heavily constrained by the *WISE* 12 band. Weingartner & Draine (2001) computed seven different grain size distributions for dust grains in the diffuse ISM of the MW, which are used in DL. The models in this "MW3.1" series are all consistent with the average interstellar extinction law[9], but have different PAH abundances in the range $0.0047 \leq q_{\rm PAH} \leq 0.047$. Draine et al. (2007) found that the SINGS galaxies span the full range of $q_{\rm PAH}$ models computed, with a median value of $q_{\rm PAH} = 0.034$. Models are further extrapolated into a (uniformly sampled) $q_{\rm PAH}$ grid, using $\delta q_{\rm PAH} = 0.001$ intervals in the range $0 \leq q_{\rm PAH} \leq 0.10$, as described by AD12.

Each dust grain is assumed to be heated by radiation with an energy density per unit frequency

$$u_\nu = U \times u_\nu^{\rm MMP83}, \tag{1}$$

where U is a dimensionless scaling factor and $u_\nu^{\rm MMP83}$ is the ISRF estimated by Mathis et al. (1983) for the solar neighbourhood. A fraction $(1-\gamma)$ of the dust mass is assumed to be heated by starlight with a single intensity $U = U_{\rm min}$, and the remaining fraction γ of the dust mass is exposed to a power-law distribution of starlight intensities between $U_{\rm min}$ and $U_{\rm max}$, with $dM/dU \propto U^{-\alpha}$. From now on, we call these the "diffuse cloud" and the "PDR" (for photodissociation regions) components respectively. AD12 found that the observed SEDs in the NGC 628 and NGC 6946 galaxies are consistent with DL models with $U_{\rm max} = 10^7$. Given the limited number of photometric constraints, we will use only models with $U_{\rm max} = 10^7$ and also fix $\alpha = 2$, a typical value found in AD12. The DL models presented in DL07 are further interpolated into a (finely sampled) $U_{\rm min}$ grid using $\delta U_{\rm min} = 0.01$ intervals, as described by A14.

Therefore, in the present work the DL parameter grid has only four dimensions, Σ_{M_d}, $q_{\rm PAH}$, $U_{\rm min}$, and γ. We explore the ranges $0.00 \leq q_{\rm PAH} \leq 0.10$, $0.01 \leq U_{\rm min} \leq 30$, and $0 \leq \gamma \leq 1.0$. For each model, the DL model library contains the model SED in a finely-spaced wavelength grid with for $1\,\mu{\rm m} < \lambda < 1{\rm cm}$.

As a derived parameter, we define the ratio

$$f_{\rm PDR} \equiv \frac{L_{\rm PDR}}{L_{\rm dust}}, \tag{2}$$

where $L_{\rm PDR}$ is the luminosity radiated by dust in regions where $U > 10^2$ and $L_{\rm dust}$ is the total power radiated by the dust. Clearly, $f_{\rm PDR}$ depends on the fitting parameter γ in the numerator and, through the denominator, also depends on $U_{\rm min}$. Dust heated with $U > 10^2$ will emit predominantly in the $\lambda < 100\,\mu$m range; therefore, the *IRAS* 60 to *IRAS* 100 intensity ratio can be increased to very high values by taking $f_{\rm PDR} \to 1$. Conversely, for a given $U_{\rm min}$, the minimum *IRAS* 60/*IRAS* 100 intensity ratio will correspond to models with $f_{\rm PDR} = 0$.

Another derived quantity, the mass-weighted mean starlight heating intensity $\langle U \rangle$, for $\alpha = 2$, is given by

$$\langle U \rangle = (1-\gamma)\,U_{\rm min} + \gamma\,U_{\rm min}\,\frac{\ln(U_{\rm max}/U_{\rm min})}{1 - U_{\rm min}/U_{\rm max}}. \tag{3}$$

Adopting the updated carbonaceous and astrosilicate densities recommended by DA14, the DL model used here is consis-

[8] For the size distribution in the DL models, the mass fraction contributed by PAH particles containing $N_C < 10^6$ C atoms is 1.478 $q_{\rm PAH}$.

[9] In the details of their size distributions and dust composition (e.g., the lack of ices), these models will not be as appropriate for dust in dark molecular clouds.

tent with the MW ratio of visual extinction to H column density, $A_V/N_{\rm H} = 5.34 \times 10^{-22}$ mag cm^2 (i.e., $N_{\rm H}/E(B-V) = 5.8 \times 10^{21}$ cm^{-2} mag^{-1}, Bohlin et al. 1978), for a dust to H mass ratio $\Sigma_{M_{\rm d}}/N_{\rm H} m_{\rm H} = 0.0091$. The dust surface density corresponds to

$$A_V = 0.74 \left(\frac{\Sigma_{M_{\rm d}}}{10^5 {\rm M}_\odot \, {\rm kpc}^{-2}} \right) {\rm mag} \, . \quad (4)$$

3.2. Fitting strategy and implementation

For each individual pixel, we find the DL parameters $\{\Sigma_{M_{\rm d}}, q_{\rm PAH}, U_{\rm min}, \gamma\}$ that minimize

$$\chi^2 \equiv \sum_k \frac{[S_{\rm obs}(\lambda_k) - S_{\rm DL}(\lambda_k)]^2}{\sigma^2_{\lambda_k}} \, , \quad (5)$$

where $S_{\rm obs}(\lambda_k)$ is the observed flux density per pixel, $S_{\rm DL}(\lambda_k)$ is the DL emission SED convolved with the filter k response function, and σ_{λ_k} is the $1\,\sigma$ uncertainty in the measured intensity density at wavelength λ_k. We use a strategy similar to that of AD12 and define σ_{λ_k} as a sum in quadrature of five uncertainty sources:

- the calibration uncertainty (proportional to the observed intensity);
- the zero-level "offset" uncertainty;
- the residual dipole uncertainty;
- CIB anisotropies;
- the instrumental noise.

Values for these uncertainties (except the noise) are given in Table 1. To produce the best-fit parameter estimates, we fit the DL model to each pixel independently of the others.

We observe that for a given set of parameters $\{q_{\rm PAH}, U_{\rm min}\}$, the model emission is bi-linear in $\{\Sigma_{M_{\rm d}}, \gamma\}$. This allows us to easily calculate the best-fit values of $\{\Sigma_{M_{\rm d}}, \gamma\}$ for a given parameter set $\{q_{\rm PAH}, U_{\rm min}\}$. Therefore, when looking for the best-fit model in the full four-dimensional model parameter space $\{\Sigma_{M_{\rm d}}, q_{\rm PAH}, U_{\rm min}, \gamma\}$, we only need to perform a search over the two-dimensional subspace spanned by $\{q_{\rm PAH}, U_{\rm min}\}$. The DL model emission convolved with the instrumental bandpasses, $S_{\rm DL}(\lambda_k)$, were pre-computed for a $\{q_{\rm PAH}, U_{\rm min}\}$ parameter grid, allowing the multi-dimensional search for optimal parameters to be performed quickly by brute force, without relying on nonlinear minimization algorithms.

In order to determine the uncertainties on the estimated parameters in each pixel, we proceed as follows: we simulate 100 observations by adding noise to the observed data; we fit each simulated SED using the same fitting technique as for the observed SED; and we study the statistics of the fitted parameters for the various realizations. The noise added in each pixel is a sum of the five contributions listed in the previous paragraph, each one assumed to be Gaussian distributed. We follow a strategy similar to that of AD12, taking a pixel-to-pixel independent contribution for the data noise and correlated contributions across the different pixels for the other four sources of uncertainty. For simplicity, we assume that none of the uncertainties are correlated across the bands. The parameter error estimate at a given pixel is the standard deviation of the parameter values obtained for the simulated SEDs. For typical pixels, the uncertainty on the estimated parameters is a few percent of their values (e.g., Figure 2 shows the signal-to-noise (S/N) ratio of $\Sigma_{M_{\rm d}}$).

4. Dust modelling results, robustness, and validation

4.1. Parameter maps

The maps of the model best-fit parameters trace Galactic structures. Galactic molecular cloud complexes are resolved and, in addition, several extended extragalactic sources are present (e.g., M31, discussed in Appendix A). Figure 1 shows the all-sky maps of the fitted dust parameters. The left column corresponds to a Mollweide projection of the sky in Galactic coordinates, and the centre and right columns correspond to orthographic projections of the southern and northern hemispheres, centred on the corresponding Galactic poles.

A14 presents the corrected *WISE* data and $q_{\rm PAH}$ maps. The mass fraction in the PAH grains is relatively small, and therefore, variations in $q_{\rm PAH}$ do not have a major impact on the $\Sigma_{M_{\rm d}}$ and optical extinction A_V estimates. If instead of using the *WISE* data to constrain $q_{\rm PAH}$, we simply fix $q_{\rm PAH} = 0.04$, the $\Sigma_{M_{\rm d}}$ and A_V estimates will only change by a few percent.

The $f_{\rm PDR}$ map shows artefact structures aligned with the ecliptic plane especially at high Galactic and low ecliptic latitudes. These artefacts are likely to be caused by residual zodiacal light in the *IRAS* 60 maps. As shown in Section 4.3.1, the dust mass estimates are not strongly biased in these regions.

Figure 2 shows a map of the dust emitted luminosity surface density, $\Sigma_{L_{\rm d}}$, the mean intensity heating the dust, $\langle U \rangle$, the χ^2 per degree of freedom (dof) of the fit, χ^2/Ndof, and a map of the S/N ratio of the dust mass surface density $\Sigma_{M_{\rm d}}$.

The χ^2/Ndof map scatter around unity in the high Galactic latitude areas, where the data uncertainties are noise-dominated. The χ^2/Ndof is slightly larger than 1 in the inner Galactic disk and several other localized areas. In the outer Galactic disk the χ^2/Ndof is smaller than 1, presumably due to overestimation of the uncertainties. Over much of the sky the fit to the FIR SED is not as good as in *Pl*-MBB; there the MBB fit has three fitting parameters in contrast with the DL model which has only two, $\Sigma_{M_{\rm d}}$ and $U_{\rm min}$[10].

4.2. Dust model photometric performance: residual maps

As shown in the χ^2/Ndof map in Figure 2, the DL model fits the observed SED satisfactorily (within $1\,\sigma$) over most of the sky areas. However, the model SEDs have systematic departures from the observed SED in the inner Galactic disk, at low ecliptic latitude, and in localized regions. The departures of the model in the low ecliptic latitude regions could be caused by defects in the zodiacal light estimation (and removal) in the photometric maps that the model cannot accommodate. In the Magellanic Clouds (MC) the DL model fails to fit the data[11]. The MC exhibit surprisingly strong emission at submm and millimetre wavelengths. Planck Collaboration XVII (2011) conclude that conventional dust models cannot account for the observed $600 - 3\,000\,\mu$m emission without invoking unphysically large amounts of very cold dust. (Draine & Hensley 2012) suggest that magnetic dipole emission from magnetic grain materials could account for the unusually strong submm emission from the Small MC.

[10] The $q_{\rm PAH}$ parameter does not affect significantly the FIR SED; it only affects significantly the *WISE* 12 photometry. The $f_{\rm PDR}$ parameter affect mostly IRAC 60 photometry, without contributing significantly to the remaining FIR bands.

[11] The MC appear as two red spots in the southern hemisphere in the top row of Figure 4

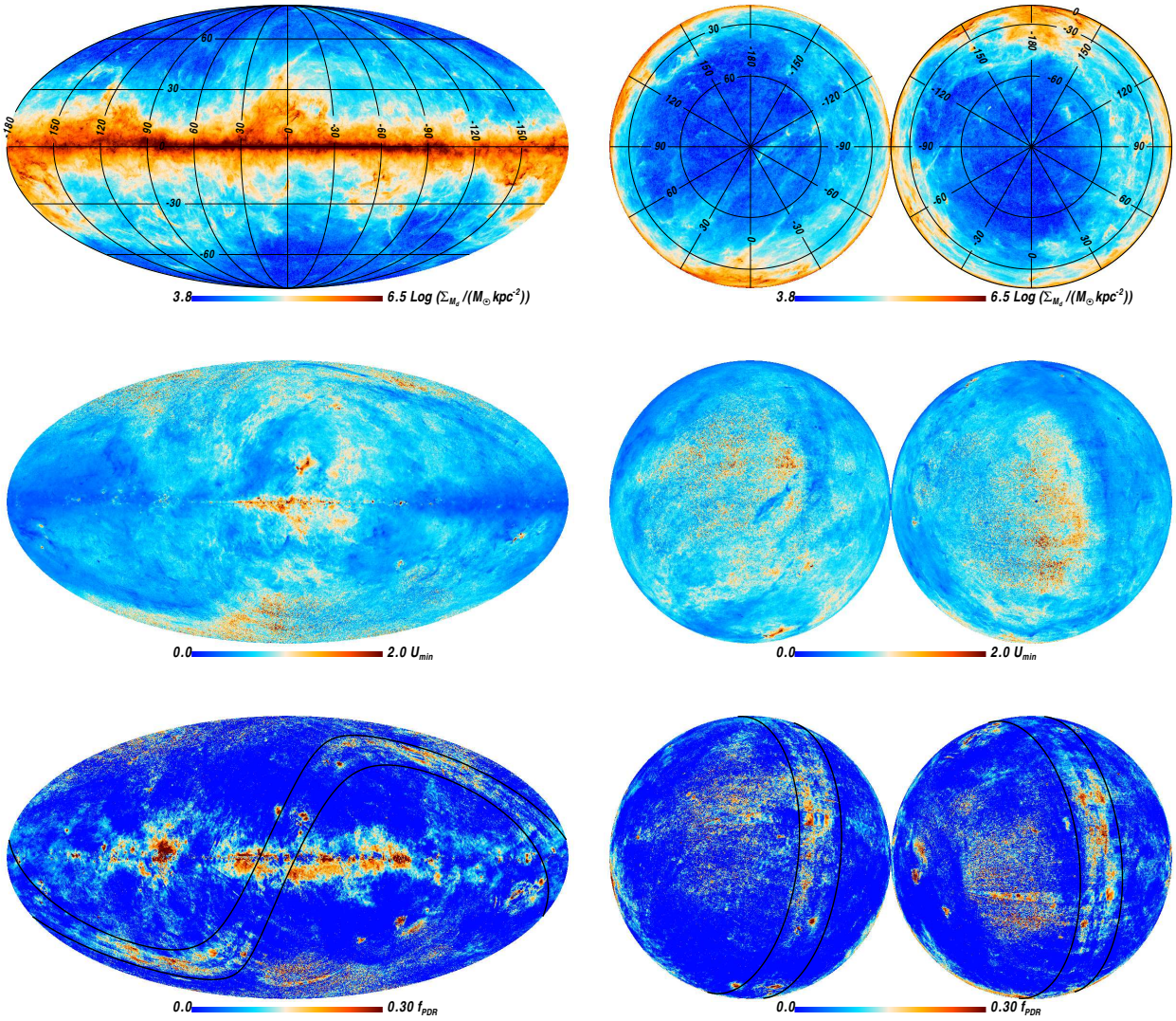

Fig. 1. DL fitted parameter maps. The top row corresponds to the dust mass surface density, Σ_{M_d}, the middle row to the mass-weighted mean starlight intensity heating the dust, $U_{\rm min}$, and the bottom row to the fraction of dust luminosity emitted by dust heated with high stellar intensities, $f_{\rm PDR}$. The left column corresponds to a Mollweide projection of the sky in Galactic coordinates, and the centre and right columns correspond to orthographic projections of the southern and northern hemispheres centred on the corresponding Galactic poles. A Galactic coordinate grid is plotted in the maps of the first row. Lines of ecliptic latitude at ±10° are plotted in the maps of the bottom row.

Figures 3 and 4 show the model departures from the photometric constraints used in the fits. Each panel shows the difference between the model predicted intensity and the observed intensity, divided by the observed uncertainty. The systematic departures show that the physical model being used does not have sufficient parameters or flexibility to fit the data perfectly.

By increasing γ (i.e., the PDR component), the DL model can increase the *IRAS* 60 to *IRAS* 100 ratio to high values, without contributing much to the *Planck* intensities. Thus, in principle, the model should never underpredict the *IRAS* 60 emission. Figure 3 shows the model performance for fitting the *IRAS* bands; several high latitude areas (mostly with $f_{\rm PDR} = 0$) have *IRAS* 60 overpredicted and *IRAS* 100 underpredicted. Both model components (the diffuse cloud and PDR components) have an *IRAS* 60 / *IRAS* 100 intensity ratio slightly larger than the ratio observed in these regions. There are several areas where the *IRAS* 60 / *IRAS* 100 ratio is below the value for the best-fit $U_{\rm min}$, hence in these areas the model (with $f_{\rm PDR} = 0$) overpredicts *IRAS* 60. This systematic effect is at the $1-2\,\sigma$ level (i.e., 10 – 20 %).

In the inner Galactic disk the DL model tends to underpredict the 350 μm and overpredict the 850 μm emission (see Figure 4). The observed SED is systematically steeper than the DL SED in the 350 – 850 μm range (i.e., between *Planck* 857 and *Planck* 353). Similar results were found in the central kiloparsec of M31 in the 250−500 μm range (DA14). The MBB fit of these regions, presented in *Pl*-MBB, finds larger values of the opacity spectral index β ($\beta \approx 2.2$) than the typical value found in the low-and mid-range dust surface density areas ($\beta \approx 1.65$). The DL SED peak can be broadened by increasing the PDR component (i.e., by raising γ or $f_{\rm PDR}$), but it cannot be made steeper than the $\gamma = 0$ ($f_{\rm PDR} = 0$) models, and the model therefore fails to fit the 350 – 850 μm SED in these regions.

Following DA14, we define

$$\Upsilon_{\rm DL} = \frac{\log(\kappa_{\rm DL} * F857/\kappa_{\rm DL} * F353)}{\log(857{\rm GHz}/353{\rm GHz})}, \qquad (6)$$

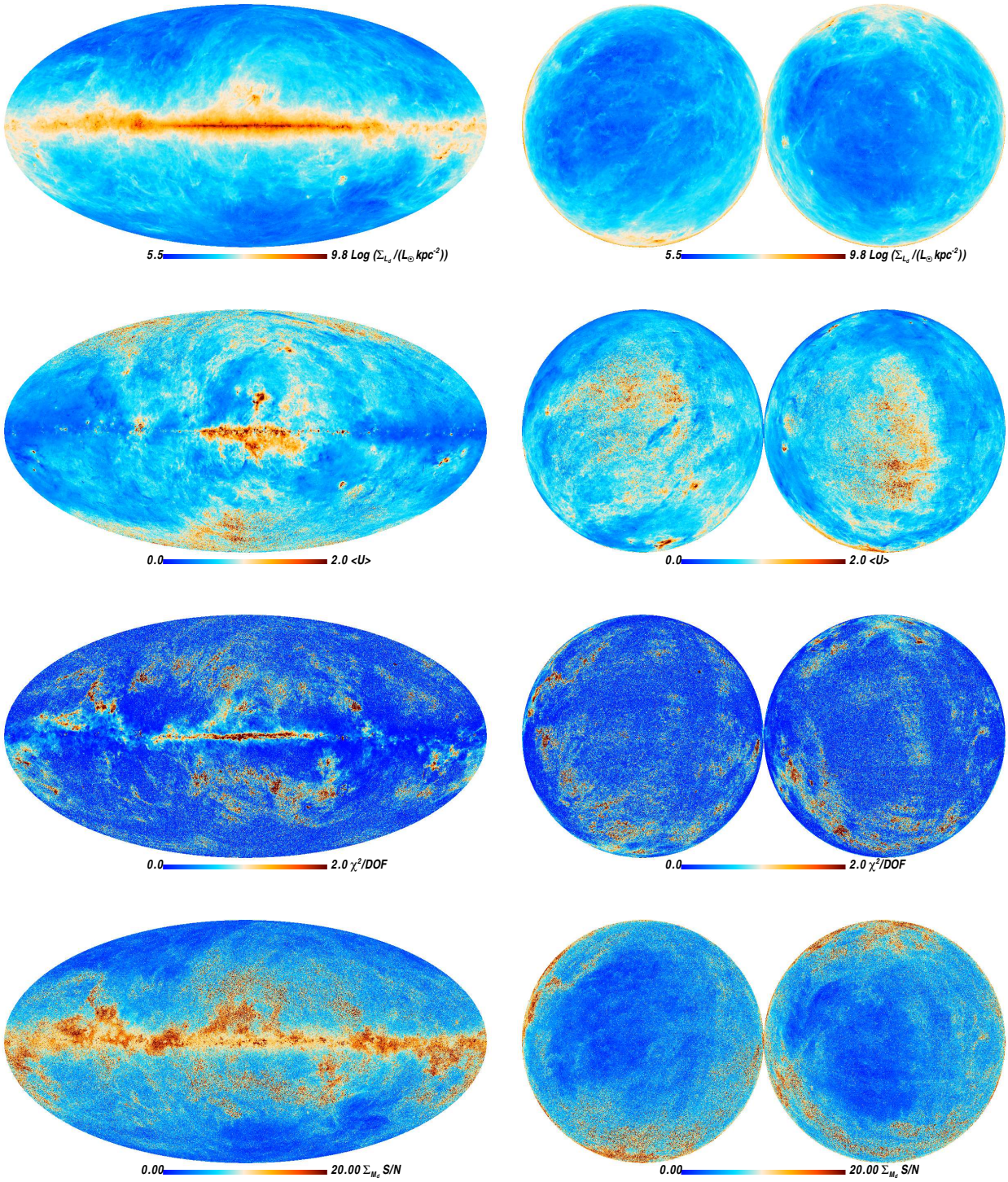

Fig. 2. DL derived parameters. The top row corresponds to the dust luminosity surface density, Σ_{L_d}, the second row shows the mean intensity heating the dust, $\langle U \rangle$, the third row shows the χ^2 per degree of freedom of the fit, χ^2/Ndof, and the bottom row the S/N map of the dust mass surface density Σ_{M_d}.

as the effective power-law index of the DL dust opacity between 350 μm and 850 μm, where $\kappa_{\rm DL} * F$ is the assumed absorption cross-section per unit dust mass convolved with the respective *Planck* filter. For the DL model[12] this ratio is $\Upsilon_{\rm DL} \approx 1.8$. We define

$$\Upsilon_{\rm Planck} = \frac{\log[I_\nu(Planck\ 857)/I_\nu(Planck\ 353)]}{\log(857{\rm GHz}/353{\rm GHz})}. \quad (7)$$

If the dust temperatures in the fitted DL model were left unchanged, then the predicted *Planck* 857/*Planck* 353 intensity ratio could be brought into agreement with observations if $\Upsilon_{\rm DL}$ were changed by $\delta\Upsilon = \Upsilon_{\rm Planck} - \Upsilon_{\rm DL}$. Figure 5 shows the $\delta\Upsilon$

[12] If the *Planck* filters were monochromatic at the nominal frequencies, then $\Upsilon_{\rm DL} = 1.82$ (see Table 2 in DA14). For the real *Planck* filters the $\Upsilon_{\rm DL}$ value is a constant close to 1.8.

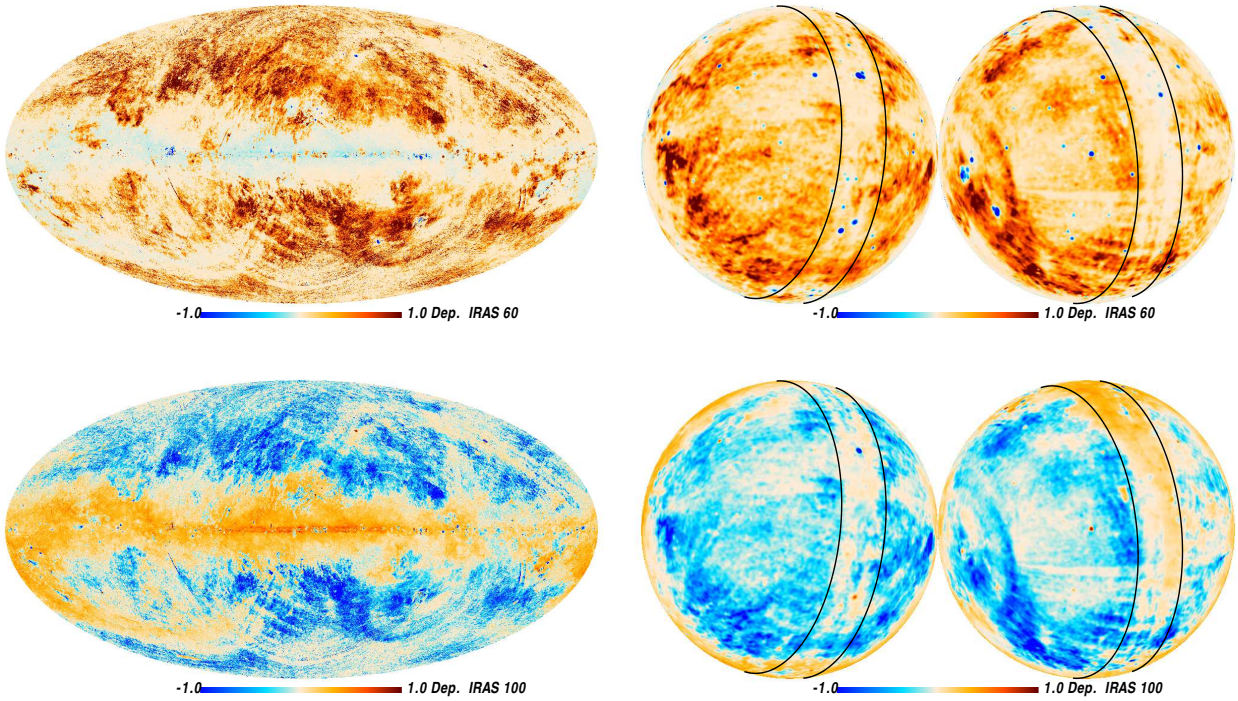

Fig. 3. Comparison between the model and the *IRAS* data used to constrain the fit. Each panel shows the model departure from the data defined as Dep. = (Model − Map)/Uncertainty. The top row corresponds to *IRAS* 60, and the bottom row to *IRAS* 100. The polar projection maps are smoothed to 1° resolution to highlight the systematic departures, and lines of Ecliptic latitude at ±10° are added for reference.

map, i.e., the opacity corrections that would bring the DL SED into agreement with the observed SED *if* the dust temperature distribution is left unchanged. The observed SED is steeper than the DL model in the inner Galactic disk ($\delta\Upsilon_{\rm DL} \approx 0.3$) and shallower in the MC ($\delta\Upsilon_{\rm DL} \approx -0.3$). Clearly, modifying the dust opacity would change the dust emission, and therefore the dust temperature distribution. Therefore, the $\delta\Upsilon$ map should be regarded as a guide on how to modify the dust opacity in future dust models, rather than as the exact correction to be applied to the opacity law per se. In the low-and mid-range surface density areas $\delta\Upsilon \approx 0.1$, while $\delta\Upsilon \approx 0.3$ in the inner Galactic disk. The large dispersion of the pixels in the low surface brightness areas is mainly due to instrumental noise. The dispersion in the large surface brightness areas may be an indicator of dust evolution, i.e., variations in the optical or FIR properties of the dust grains in the diffuse ISM.

4.3. Robustness of the mass estimate

4.3.1. Importance of *IRAS* 60

To study the potential bias introduced by *IRAS* 60, due to a possible non ideal zodiacal light estimation (whose relative contribution is the largest in the *IRAS* 60 band) or the inability of the DL model to reproduce the correct SED in this range, one can perform modelling without the *IRAS* 60 constraint. In this case we set $\gamma = 0$, i.e., we allow only the diffuse cloud component ($f_{\rm PDR} = 0$), and so we have a two-parameter model.

Figure 6 shows the ratio of the dust mass estimated without using the *IRAS* 60 constraint and with $\gamma = 0$ to that estimated using *IRAS* 60 and allowing γ to be fitted (i.e., our original modelling). The left panel shows all the sky pixels and the right panel only the pixels with $f_{\rm PDR} > 0$. In the mid-and-high-range surface mass density areas ($\Sigma_{M_{\rm d}} > 10^5 {\rm M}_\odot\,{\rm kpc}^{-2}$), where the photometry has good S/N, both models agree well, with a rms scatter below 5 %. The inclusion or exclusion of the *IRAS* 60 constraint does not significantly affect our dust mass estimates in these regions. In the low surface density areas, inclusion of the *IRAS* 60 does not change the $\Sigma_{M_{\rm d}}$ estimate in the $f_{\rm PDR} > 0$ areas, but it leads to an increase of the $\Sigma_{M_{\rm d}}$ estimate in the $f_{\rm PDR} = 0$ pixels. In the $f_{\rm PDR} = 0$ areas, the model can overpredict *IRAS* 60 in some pixels, and therefore, when this constraint is removed, the dust can be fitted with a larger $U_{\rm min}$ value reducing the $\Sigma_{M_{\rm d}}$ needed to reproduce the remaining photometric constraints. In the $f_{\rm PDR} > 0$ areas, the PDR component has a small contribution to the longer wavelengths constraints, and therefore removing the *IRAS* 60 constraint and PDR component has little effect in the $\Sigma_{M_{\rm d}}$ estimates.

4.3.2. Dependence of the mass estimate on the photometric constraints

The *Planck* and *IRAS* data do not provide photometric constraints in the $120\,\mu{\rm m} < \lambda < 300\,\mu{\rm m}$ range. This is a potentially problematic situation, since the dust SED typically peaks in this wavelength range. We can add the DIRBE 140 and DIRBE 240 constraints in a low resolution (FWHM $>$ 42′) modelling to test this possibility.

We compare two analyses performed using a 1° FWHM Gaussian PSF. The first uses the same photometric constraints as the high resolution modelling (*WISE*, *IRAS*, and *Planck*), and the second additionally uses the DIRBE 140 and DIRBE 240 constraints. The results are shown in Figure 7. Both model fits agree very well, with differences between the dust mass estimates of only a few percent. Therefore, our dust mass estimates are not substantially affected by the lack of photometric constraints near the SED peak. This is in agreement with similar tests carried out in *Pl*-MBB.

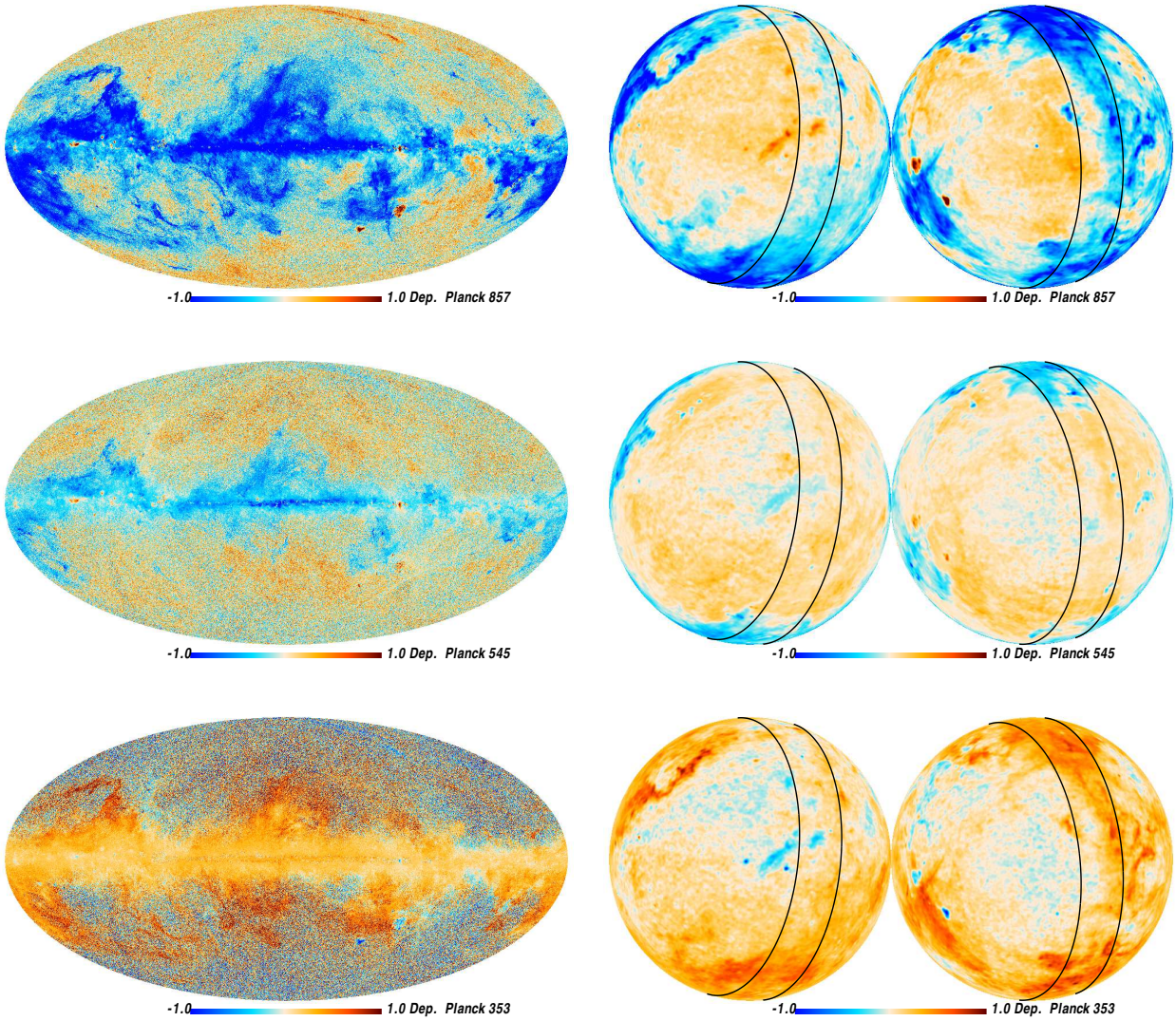

Fig. 4. Comparison between the model and the *Planck* data used to constrain the fit. Each panel shows the model departure from the data defined as Dep. = (Model - Map)/Uncertainty. The top row correspond to *Planck* 857, the central row to *Planck* 545, and the bottom row to *Planck* 353. The polar projection maps are smoothed to 1° resolution to highlight the systematic departures, and lines of Ecliptic latitude at ±10° are added for reference.

4.4. Validation on M31

In Appendix A we compare our dust mass estimates in the Andromeda galaxy (M31) with estimates based on an independent data set and processing pipelines. Both analyses use the DL model. This comparison allows us to analyse the impact of the photometric data used in the dust modelling. We conclude that the model results are not sensitive to the specific data sets used to constrain the FIR dust emission, validating the present modelling pipeline and methodology.

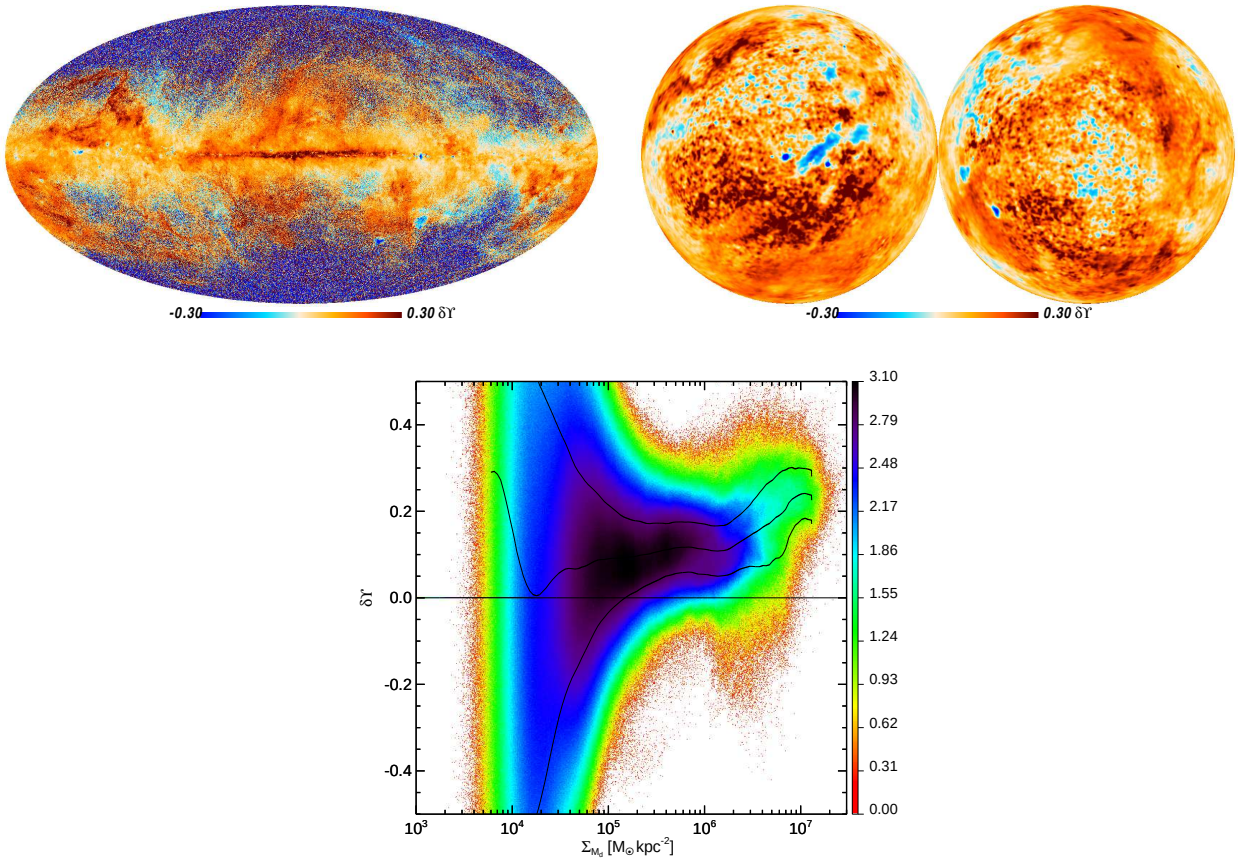

Fig. 5. Correction to the FIR opacity power law-index ($\delta\Upsilon$) needed to bring the DL SED into agreement with the *Planck* observations. The polar projection maps are smoothed to 1° resolution to highlight the systematic departures. The bottom row shows the scatter of the $\delta\Upsilon$ map as a function of Σ_{M_d}. Colour corresponds to the logarithm of the density of points, i.e., the logarithm of number of sky pixels that have a given (Σ_{M_d}, $\delta\Upsilon$) value in the plot. The curves correspond to the mean value and the $\pm 1\,\sigma$ dispersion.

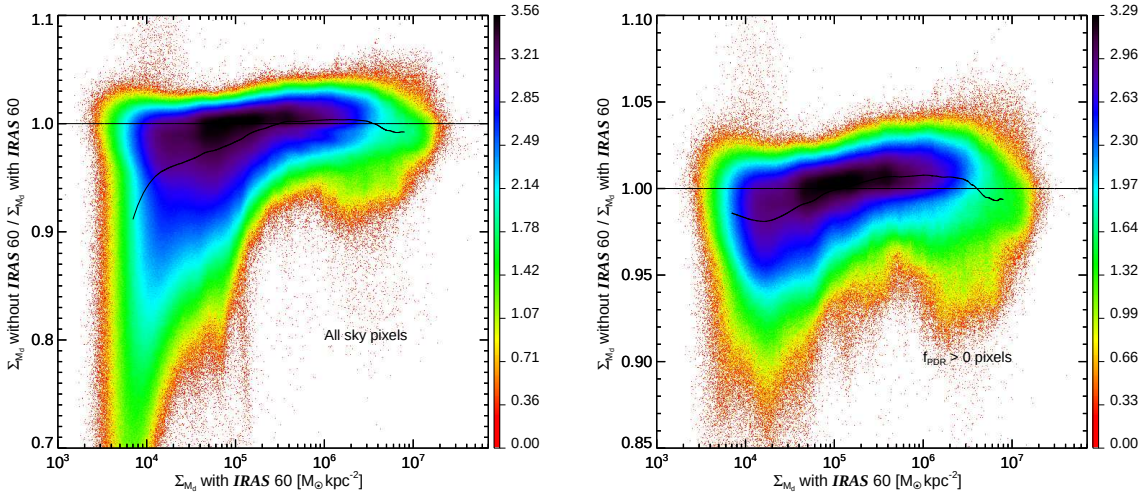

Fig. 6. Comparison between the dust mass estimates when the *IRAS* 60 constraint is excluded or included in the fit. The left panel show all the sky pixels, and the right panel only the $f_{\rm PDR} > 0$ pixels. The vertical axis corresponds to the ratio of the inferred mass density of a fit *without* using the *IRAS* 60 constraint to that obtained when this constraint is present (see text). Colour corresponds to the logarithm of the density of points (see Figure 5). The horizontal curve correspond to the mean value.

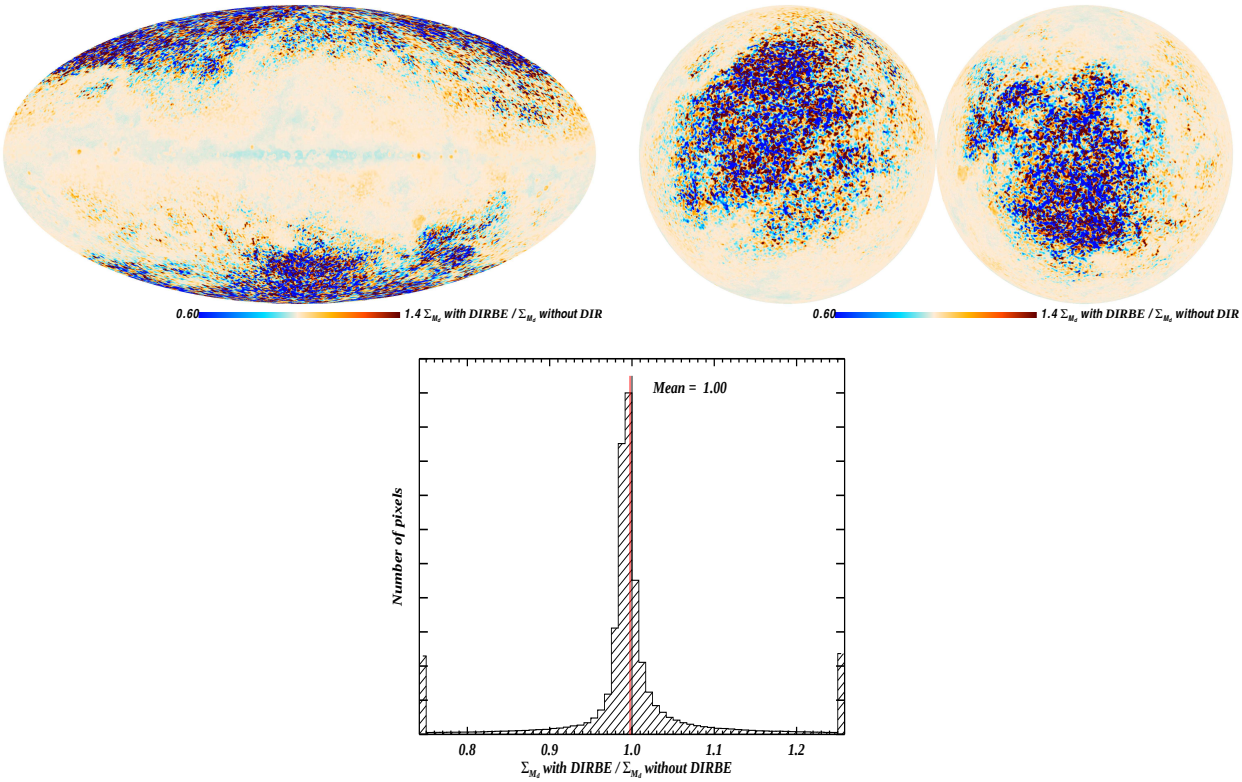

Fig. 7. Comparison between the dust mass estimates obtained with and without the DIRBE 140 and DIRBE 240 photometric constraints. The top row shows maps of the ratio between the two dust mass estimates, and the bottom row shows the corresponding histogram. Both model fits are performed using a 1° FWHM Gaussian PSF. The difference between the dust mass estimates is relatively small (within a few percent) and so it is safe to perform a modelling of the sky without the DIRBE constraints. In the bottom row, the points below 0.8 and over 1.2 were added to the 0.8 and 1.2 bars, respectively.

5. Comparison between the DL and MBB results

We now compare the DL optical extinction estimates with the estimates from the MBB dust modelling presented in *Pl*-MBB, noted $A_{V,\mathrm{DL}}$ and $A_{V,\mathrm{MBB}}$ respectively. Both estimates are based on the same *Planck* and *IRAS* 100 data, but our DL modelling also includes *IRAS* 60 and *WISE* 12 constraints. The DL model has two extra parameters (γ and q_{PAH}) that can adjust the *IRAS* 60 and *WISE* 12 intensity fairly independently of the remaining bands. Therefore, the relevant data that both models are using in determining the FIR emission are essentially the same. The MBB extinction map has been calibrated with external (optical) observational data, and so this comparison allows us to test the DL modelling against those independent data.

Pl-MBB estimated the optical extinction[13] $A_{V,\mathrm{QSO}}$ for a sample of QSOs from the Sloan Digital Sky Survey (SDSS) (York et al. 2000). A single normalization factor Π was chosen to convert their optical depth τ_{353} map (the parameter of the MBB that scales linearly with the total dust emission, similar to the DL $\Sigma_{M_{\mathrm{d}}}$) into an optical extinction map: $A_{V,\mathrm{MBB}} \equiv \Pi\,\tau_{353}$.

DL is a physical dust model and therefore fitting the observed FIR emission directly provides an optical extinction estimate, without the need for an extra calibration. However, if the DL dust model employs incorrect physical assumptions (e.g., the value of the FIR opacity), it may systematically over or under estimate the optical extinction corresponding to observed FIR emission.

Figure 8 shows the ratio of the DL and MBB A_V estimates. The top row shows the ratio map. The bottom row shows its scatter and histogram. Over most of the sky ($0.1\,\mathrm{mag} < A_{V,\mathrm{DL}} < 20\,\mathrm{mag}$), the $A_{V,\mathrm{DL}}$ values are larger than the $A_{V,\mathrm{MBB}}$ by a factor of 2.40 ± 0.40. This discrepancy is roughly independent of $A_{V,\mathrm{DL}}$. The situation changes in the very dense areas (inner Galactic disk). In these areas ($A_{V,\mathrm{DL}} \approx 100\,\mathrm{mag}$), the $A_{V,\mathrm{DL}}$ are larger than the $A_{V,\mathrm{MBB}}$ estimates by 1.95 ± 0.10.

In the diffuse areas ($A_{V,\mathrm{DL}} \lesssim 1$), where the $A_{V,\mathrm{MBB}}$ has been calibrated using the QSOs, $A_{V,\mathrm{DL}}$ overestimates the $A_{V,\mathrm{MBB}}$ values, and therefore $A_{V,\mathrm{DL}}$ should overestimate the $A_{V,\mathrm{QSO}}$ by a similar factor. The optical extinction overestimation arises from two factors.

- The DL dust physical parameters were chosen so that the model reproduces the SED proposed by Finkbeiner et al. (1999), based on FIRAS observations. It was tailored to fit the high latitude $I_\nu/N(\mathrm{H_I})$ with $U_{\min} \approx 1$. The high latitude SED from *Planck* observations differs from that derived from FIRAS observations. The difference depends on the frequency and can be as high as 20 % (Planck Collaboration VIII 2014). The best fit to the mean *Planck* + *IRAS* SED on the QSO lines of sight is obtained for $U_{\min} \approx 0.66$. The dust total emission (luminosity) of *Planck* observations and the Finkbeiner et al. (1999) SED are similar. The dust total emission per unit of optical reddening (or mass) scales linearly with $U_{\min}$. Therefore, we need $1/0.66 \approx 1.5$ more dust mass to reproduce the observed luminosity. This is in agreement with the results of Planck Collaboration Int. XVII (2014) who have used the dust - $\mathrm{H_I}$ correlation at high Galactic latitudes to measure the dust SED per unit of $\mathrm{H_I}$ column density. They find that their SED is well fit by the DL model for $U_{\min} = 0.7$ after scaling by a factor 1.45.
- The optical extinction per gas column density used to construct the DL model is that of Bohlin et al. (1978). Recent observations show that this ratio needs to be decreased by a factor of approximately $1/1.4$ (Liszt 2014a,b).

Therefore, we expect the $A_{V,\mathrm{DL}}$ to overestimation the $A_{V,\mathrm{QSO}}$ by ≈ 2.1. In Section 6.2 we proceed to make a more direct estimation.

We observe that the standard deviation of $A_{V,\mathrm{DL}}/A_{V,\mathrm{MBB}}$ in the QSO lines of sight is 10 %, and therefore the relatively large systematic variations in the ratio of the $A_{V,\mathrm{DL}}/A_{V,\mathrm{QSO}}$ versus $U_{\min}$ (that will be discussed in Section 8) should also be present in the MBB fit. Other existing dust models also have similar systematic variations in the ratio of their predicted A_V to the $A_{V,\mathrm{QSO}}$ versus $U_{\min}$.

In the inner Galactic disk the DL emissivity is shallower than the observed SED ($\delta\Upsilon \approx 0.3$, see Section 4.2). The DL emissivity is fixed and its SED cannot be adjusted to match the observed SED closely, while the MBB model (with one extra effective degree of freedom) fits the observed SED better in these regions. Neither the $A_{V,\mathrm{MBB}}$ values nor the $A_{V,\mathrm{DL}}$ values were externally calibrated in these regions.

6. Variation in optical extinction to FIR emission in diffuse areas: QSO analysis

We seek to understand whether the overestimation of the optical extinction per unit of FIR emission for the DL model (by a factor of 2.4) is constant across the sky, or if it depends on the model parameters. We describe the motivations of the analysis and QSO sample to be used in Sect. 6.1. We compare the DL and QSO A_V estimates ($A_{V,\mathrm{DL}}$, $A_{V,\mathrm{QSO}}$) in Sect. 6.2. We use the results of this analysis to propose a renormalization of the DL model that compensates for the systematic departures found across the sky in Section 6.3. We provide the observed FIR SEDs per unit of optical extinction set in Section 6.4. Finally, we discuss the ability of the DL model to fit the proposed SEDs in Section 6.5.

6.1. The QSO sample

We estimate $A_{V,\mathrm{QSO}}$ and proceed to compare the $A_{V,\mathrm{DL}}$ and $A_{V,\mathrm{QSO}}$ estimates directly, and study the discrepancies as a function of the DL parameter $U_{\min}$.

SDSS provides a sample of 272 366 QSOs that allows us to study the optical properties of Galactic dust. A subsample of 105 783 (an earlier data release) was used in *Pl*-MBB to normalize the opacity maps derived from the MBB fits in order to produce an extinction map.

The use of QSOs as calibrators has several advantages over other cross-calibrations:

- QSOs are extragalactic, and at high redshift, so all the detected dust in a given pixel is between the QSO and us, a major advantage with respect to maps generated from stellar reddening studies;
- the QSO sample is large and well distributed across diffuse ($A_V \lesssim 1$) regions at high Galactic latitude, providing good statistics;
- SDSS photometry is very accurate and well understood.

In Appendix B we describe the SDSS QSO catalogue in detail, and how for each QSO we measure the extinction $A_{V,\mathrm{QSO}}$

[13] *Pl*-MBB actually determine optical reddening $E(B-V)$ for the QSO sample. Since a fixed extinction curve with $R_V = 3.1$ (see App. B.2) was used, this is equivalent to determining the optical extinction A_V.

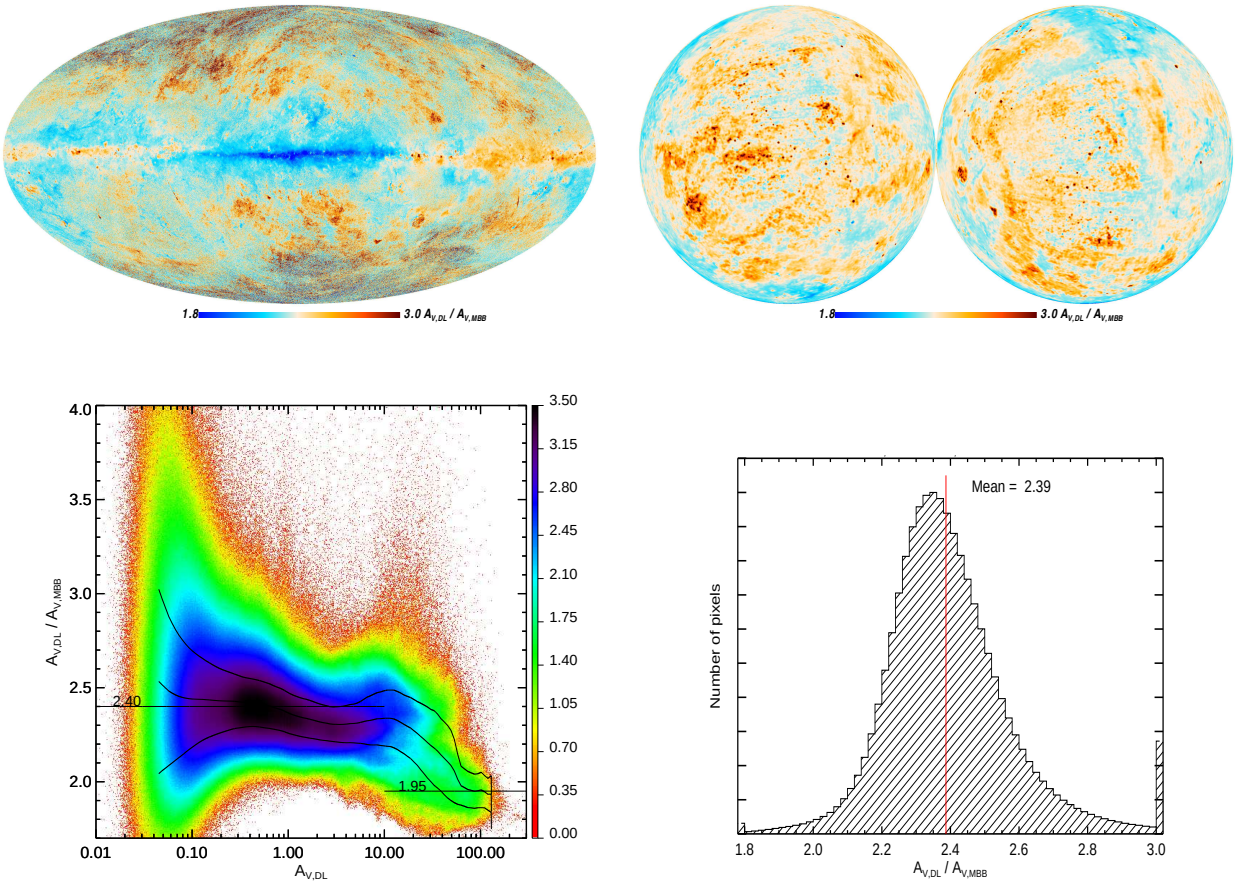

Fig. 8. Comparison between DL and MBB A_V estimates, noted $A_{V,\mathrm{DL}}$ and $A_{V,\mathrm{MBB}}$ respectively. The top row shows the ratio of the $A_{V,\mathrm{MBB}}$ and $A_{V,\mathrm{DL}}$ maps. The polar projection maps are smoothed to 1° resolution to highlight the systematic departures. The bottom row shows the ratio of the $A_{V,\mathrm{MBB}}$ and $A_{V,\mathrm{DL}}$ estimates as a function of the $A_{V,\mathrm{DL}}$ estimate (left) and its histogram (right). In the bottom left panel the colour corresponds to the logarithm of the density of points (see Figure 5). The curves correspond to the mean value and the $\pm 1\,\sigma$ dispersion. The DL and MBB analyses are based on the same data sets.

from the optical SDSS observations. For clarity, in the next section we will denote the DL extinction based on modelling the FIR emission, as $A_{V,\mathrm{DL}}$.

6.2. $A_{V,\mathrm{QSO}} - A_{V,\mathrm{DL}}$ comparison

In this section, we present a comparison of the DL and QSO extinction, as a function of the fitted parameter U_{min}. This study provides information on variations in the dust optical properties, and will allow us to gain valuable checks of the validity of the assumptions of the DL model.

Figure 9 compares the DL and QSO A_V estimates. It shows the slope $\epsilon(U_{\mathrm{min}})$ when fitting the $A_{V,\mathrm{QSO}}$ versus $A_{V,\mathrm{DL}}$ data with a line through the origin for a group of QSOs. To compute the $\epsilon(U_{\mathrm{min}})$, we sort the QSO lines of sight with respect of the U_{min} value of the Galactic dust, and divide them in 10 groups having (approximately) equal number of QSOs each. We observe that $\epsilon(U_{\mathrm{min}})$, a weighted mean of $A_{V,\mathrm{QSO}}/A_{V,\mathrm{DL}}$ in each U_{min} bin, is a strong function of U_{min}. The slope of fitting the $A_{V,\mathrm{QSO}}$ versus $A_{V,\mathrm{DL}}$ for the combined sample of QSOs is $\langle\epsilon\rangle \approx 0.52$. Therefore, on average the DL model overpredicts the observed $A_{V,\mathrm{QSO}}$ by a factor of $1/0.52 = 1.9$, with the discrepancy being larger for sightlines with smaller U_{min} values. There is a 24 % difference between the 2.4 factor that arises from the comparison between $A_{V,\mathrm{DL}}$ and $A_{V,\mathrm{QSO}}$ indirectly via the MBB A_V fit, and the factor of 1.9 found here. This is due to the use of a different QSO sample (*Pl*-MBB used a smaller QSO sample), which accounts for 10 % of the difference, and the way that the QSO A_V is computed from the SDSS photometry (see Appendix B for details), responsible of the remaining 14 %.

For a given FIR SED, the DL model predicts the optical reddening unambiguously, with no freedom for any extra calibration. However, if one had the option to adjust the DL extinction estimates by multiplying them by a single factor (i.e., ignoring the dependence of ϵ on U_{min}), one would reduce the optical extinction estimates by a factor of 0.52.

6.3. Dependence of the $A_{V,\mathrm{DL}}$ overestimation on U_{min} in the diffuse ISM

The ratio of the DL predicted extinction, based on FIR observations, to that estimated with optical photometry of QSOs is a function of U_{min}. Therefore, to have a better estimate of the optical extinction A_V, one can parametrize the model prediction departures, and adjust the A_V maps to compensate for this bias.

The optical extinction discrepancy can be approximated as a linear function of U_{min}:

$$A_{V,\mathrm{QSO}} \approx (0.31\,U_{\mathrm{min}} + 0.35)\,A_{V,\mathrm{DL}}, \qquad (8)$$

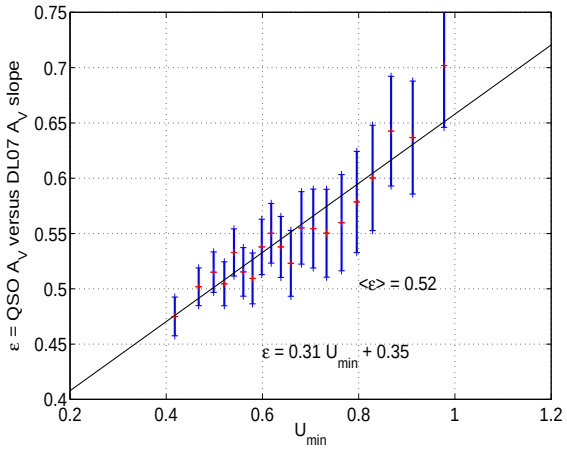

Fig. 9. Ratio between the QSO extinction estimates $A_{V,\mathrm{QSO}}$ and the DL extinction estimates $A_{V,\mathrm{DL}}$, as a function of the fitted parameter U_{min}. Empirically, the slope of $A_{V,\mathrm{QSO}}$ versus $A_{V,\mathrm{DL}}$ (ϵ) can be approximated by a linear function of U_{min}.

We define a renormalized DL optical reddening as[14]:

$$A_{V,\mathrm{RQ}} = (0.31\,U_{\mathrm{min}} + 0.35) \times A_{V,\mathrm{DL}}. \quad (9)$$

Empirically, $A_{V,\mathrm{RQ}}$ is our best estimator of the QSO extinction $A_{V,\mathrm{QSO}}$.

Pl-MBB proposed the dust radiance (the total luminosity emitted by the dust) as a tracer of dust column density in the diffuse ISM. This would be expected *if* the radiation field heating the dust were uniform, and the variations of the dust temperature were only driven by variation of the dust FIR-submm opacity in the diffuse ISM. The dust radiance is proportional to $U_{\mathrm{min}} \times A_{V,\mathrm{DL}}$. Our best fit of the renormalization factor as a function of U_{min} is an intermediate solution between the radiance and the non-renormalized model column density ($A_{V,\mathrm{DL}}$). The $A_{V,\mathrm{RQ}}$ increases with U_{min} but with a slope smaller than 1. Figure 9 shows that our renormalization is a better fit of the data than the radiance.

6.4. Observed FIR SED per unit of optical extinction

The parameter U_{min} is largely determined by the wavelength where the SED peaks; as a corollary, SEDs for different values of U_{min} differ significantly. The A_V values obtained from the QSO analysis, $A_{V,\mathrm{QSO}}$, allow us to normalize the observed SEDs (per unit of optical extinction) and generate a one-parameter family of I_ν/A_V. This family is indexed by the U_{min} parameter; the QSO lines of sight are grouped according to the fitted Galactic U_{min} value. We divide the sample of "good" QSOs in 10 bins, containing 22 424 QSOs each[15].

To obtain the I_ν/A_V values we proceed as follows. For each band and U_{min}, we would like to perform a linear regression of the I_ν values as a function of $A_{V,\mathrm{QSO}}$. The large scatter and non-Gaussian distribution of $A_{V,\mathrm{QSO}}$ and the scatter on I_ν make it challenging to determine such a slope robustly. Therefore, we smooth the maps to a Gaussian PSF with 30′ FWHM to reduce the scatter on I_ν, redo the dust modelling (to obtain a coherent U_{min} estimate), and perform the regression on the smoothed (less noisy) maps. The non-Gaussian distribution of $A_{V,\mathrm{QSO}}$ do not introduce any bias in the slope found[16].

Unfortunately, the complex statistics of the $A_{V,\mathrm{QSO}}$ estimates (that derive from variations in the QSO physical properties), makes it hard to obtain a reliable estimate of the uncertainties in the (normalizing) A_V estimates. The statistical uncertainties in the A_V estimates are rather small due to the large size of the QSOs sample: our determination of the FIR intensities per unit of optical extinction is mostly uncertain due to systematic biases. $\mathrm{H_I}$ column densities obtained from the Leiden/Argentina/Bonn 21cm (LAB) survey (Kalberla et al. 2005) for our QSO sightlines result in a mean value $N_{\mathrm{H}} = 7.7 \times 10^{21}\mathrm{cm}^{-2}\,\mathrm{E(B-V)}$, 8% smaller than the $N_{\mathrm{H}} = 8.3 \times 10^{21}\mathrm{cm}^{-2}\,\mathrm{E(B-V)}$ found by Liszt (2014b). Therefore, we infer our $A_{V,\mathrm{QSO}}$ normalization may be uncertain to about 5 – 10 %. The instrumental calibration uncertainties translate directly to the FIR intensities per unit of optical extinction. Therefore, the normalization of each SED may be uncertain to about ≈ 15 %.

Table 2 provides a set of empirical FIR intensities per unit of optical extinction, *indexed by the DL* U_{min} value. The set forms one SED for each U_{min} value. The map values for *Planck* 217 and *Planck* 143, which were not used to constrain the DL model, are also included in Table 2.

Table 2 additionally includes the $\Sigma_{L_\mathrm{d}}/A_V$ values from the DL fit. The fact that the DL fits the observed SED relatively well, makes Σ_{L_d} a good estimate of the integral of the observed SEDs, i.e., the DL SEDs are used as a tool to interpolate the intensity between the bands, and the integrated SEDs are relatively model independent. Table 2 shows that the luminosity per A_V is a monotonic function of U_{min}, and therefore luminosity is not the best tracer of A_V in the diffuse ISM; our $A_{V,\mathrm{RQ}}$ is the best tracer of A_V in the diffuse ISM.

Within each U_{min} bin, the SEDs differ due to variations in the dust properties. We normalize each SED by its DL Σ_{L_d}, and study the SEDs mean scatter around the mean SED. The last row of Table 2 presents such rms scatters. For each band, the scatters are similar for the different U_{min} bins, and therefore we quote the mean scatter for all the bins. The large scatter in *Planck* 217 and *Planck* 143 is partially due to stochastic noise in the data. The large scatter in *IRAS* 100 is due to variations in f_{PDR} between the SEDs. The scatter in the remaining bands is mainly due to variations in the dust SEDs.

Figure 10 present the set of SEDs. The left panel shows the SEDs for the different U_{min} values. The right panel shows each SED divided by the mean to highlight the differences between the individual SEDs.

6.5. DL fit to the observed FIR SED per unit of optical extinction

How does the DL model and its renormalized version compare with the new FIR constraints proposed in Sect.6.4?

The DL SED reproduces correctly the observed SED over most of the sky (see Section 4.2). Systematic departures in the low surface areas can be due to poor zodiacal light estimation in the data. Even in these areas, the departures are within the photometric uncertainties.

Figure 11 shows the measured intensity per unit of optical extinction (red crosses) for the DL prediction. The different panels correspond to the different bands: *IRAS* 100; *Planck* 857; *Planck* 545; and *Planck* 353. In each panel, the black curve corresponds to the DL predicted intensity, and the red curves to the

[14] We add the letter "Q" to indicate the renormalization using the $A_{V,\mathrm{QSO}}$.

[15] A few of the bins contain 22 425 QSOs

[16] See discussion in Appendix B.2, and Figure B.2.

Table 2. FIR observed emission per unit of optical extinction

SED #	DL fit $U_{\rm min}$	DL fit $\Sigma_{L_{\rm d}}/10^7$ [$L_\odot$ kpc^{-2}mag^{-1}]	Intensity per A_V [MJy sr^{-1} mag^{-1}] *Planck* 143	*Planck* 217	*Planck* 353	*Planck* 545	*Planck* 857	*IRAS* 100	*IRAS* 60
1	0.4178	2.28	0.0506	0.221	0.937	3.22	9.33	10.2	2.20
2	0.4674	2.33	0.0509	0.211	0.908	3.17	9.36	10.8	2.27
3	0.4984	2.39	0.0488	0.208	0.901	3.15	9.36	11.4	2.39
4	0.5207	2.54	0.0510	0.215	0.933	3.27	9.73	12.4	2.67
5	0.5407	2.46	0.0490	0.205	0.894	3.14	9.35	12.2	2.46
6	0.5602	2.62	0.0505	0.215	0.935	3.28	9.77	13.2	2.93
7	0.5793	2.73	0.0512	0.219	0.954	3.36	10.1	14.0	2.82
8	0.5984	2.65	0.0529	0.211	0.912	3.22	9.64	13.7	2.99
9	0.6182	2.67	0.0498	0.207	0.899	3.18	9.54	14.0	2.76
10	0.6383	2.80	0.0496	0.211	0.928	3.28	9.90	14.9	2.92
11	0.6590	2.98	0.0549	0.220	0.963	3.41	10.3	15.9	3.16
12	0.6810	2.89	0.0486	0.207	0.914	3.25	9.86	15.7	3.11
13	0.7056	3.01	0.0507	0.210	0.926	3.29	10.0	16.4	3.29
14	0.7333	3.14	0.0494	0.213	0.945	3.36	10.3	17.3	3.51
15	0.7644	3.35	0.0509	0.214	0.944	3.36	10.3	18.2	4.40
16	0.7960	3.23	0.0492	0.208	0.921	3.29	10.1	18.3	3.75
17	0.8289	3.21	0.0467	0.202	0.898	3.21	9.93	18.5	3.77
18	0.8673	3.13	0.0465	0.191	0.848	3.04	9.50	18.2	3.77
19	0.9123	3.31	0.0445	0.194	0.868	3.13	9.82	19.5	4.11
20	0.9776	3.27	0.0415	0.180	0.802	2.91	9.19	19.2	4.32
rms fluctuations in each bin [%]			41.30[a]	12.97[a]	4.72	3.08	4.43	7.71	29.43[b]

a The main source of fluctuations is statistical noise in the band photometry.
b The main source of fluctuations is variation of $f_{\rm PDR}$ in the lines of sight.

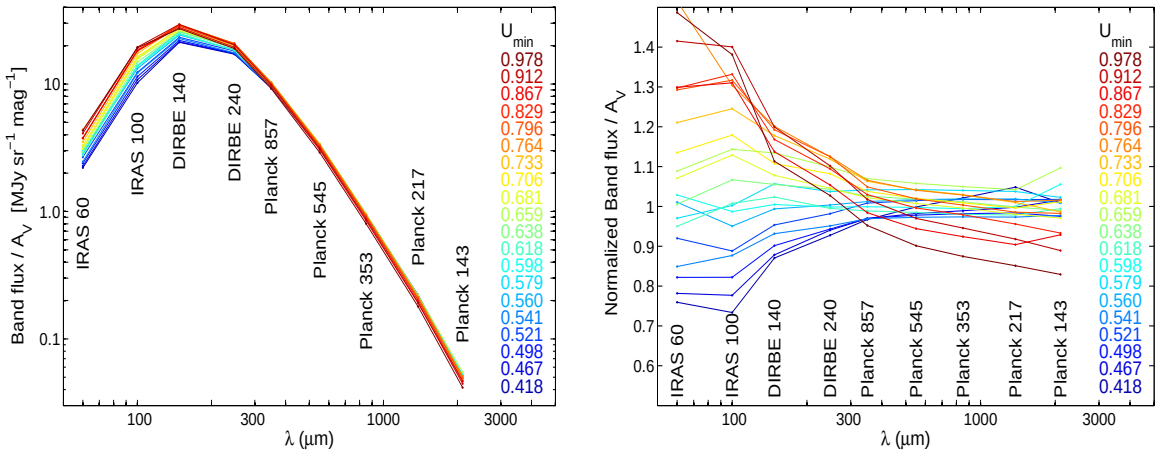

Fig. 10. FIR measured intensity per unit of optical extinction as a function of the fitted parameter $U_{\rm min}$. In the right panel, the SEDs are divided by the mean SED, i.e., normalized with the SED per unit of optical extinction obtained without binning on $U_{\rm min}$.

renormalized QDL intensity prediction. The DL model underpredicts the FIR per unit of optical extinction A_V by significant amounts, especially for sightlines with low fitted values of $U_{\rm min}$. The DL model emission is less sensitive to $U_{\rm min}$ at longer wavelengths (i.e., the black curves are more horizontal at longer wavelengths). We observe that the renormalization of the DL A_V values brings into agreement the observed and predicted band intensities per unit of extinction (red curves). *Note that the red and black curves are not the product of a fit to these data*, they correspond to the original and renormalized models respectively.

Figure 12 shows the fit of the DL model to the mean SED over the QSO lines of sight. The observed SED was computed similarly as the ones in Table 2 (performing a linear regression of the I_ν values as a function of $A_{V,\rm QSO}$), but using all the QSOs, i.e., without binning in $U_{\rm min}$. It is quite close to the mean of the SEDs presented in Table 2. The DL model fit was done using the same bands as in the main fit. DL fits the observed FIR SED within 1.7% in the *IRAS* 60, 100, *Planck* 857, *Planck* 545, and *Planck* 353 bands. Moreover the models also predicts *Planck* 217 and *Planck* 143 fluxes (not used to constrain the fit) within 1.7%. DL differs from DIRBE bands by about 6%[17]. It is remarkable that the DL spectral shape fit the *Planck* 857 – *Planck* 143 SED within 1.7%.

We conclude that the DL model has approximately the correct SED shape to fit the diffuse ISM, and a $U_{\rm min}$-dependent renormalization brings the model optical extinction into agreement with the *IRAS* and *Planck* data.

[17] The DIRBE photometry employed is not reliable: The DIRBE maps are quite noisy in the 30′ beams used to extract the observed SED.

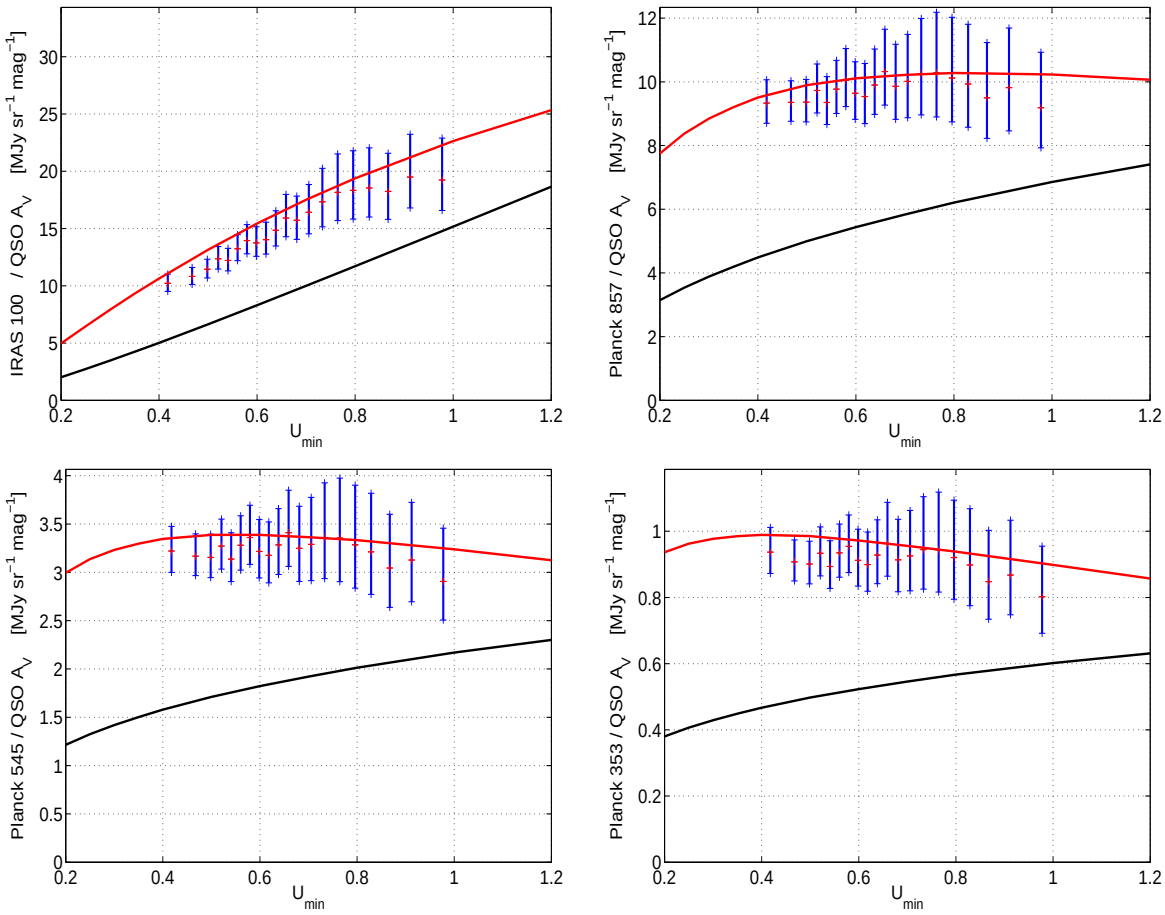

Fig. 11. FIR measured intensity per unit of optical extinction as a function of the fitted parameter $U_{\rm min}$. The top row corresponds to *IRAS* 100 (left) and *Planck* 857 (right) and the bottom row to *Planck* 545 (left) and *Planck* 353 (right). The red crosses correspond to the the values provided in Table 2. The DL predictions are plotted in black and the renormalized model (RQ) predictions in red. The renormalized QDL model predicts the FIR intensity remarkably well.

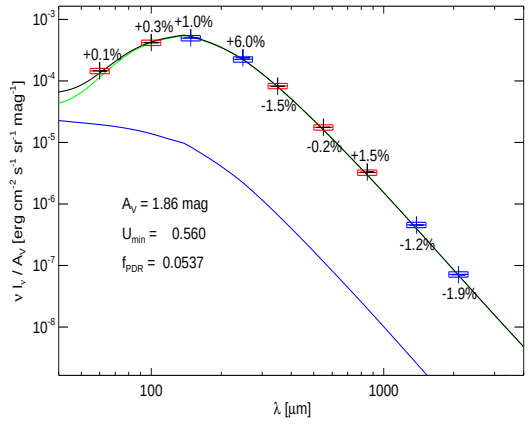

Fig. 12. DL fit to the mean SED over the QSO lines of sight. The crosses are the model predicted fluxes in the bands, the red horizontal lines are the measured flux, and red rectangles around them is a 10% uncertainties. The red symbols correspond to *IRAS* 60, 100, *Planck* 857, 545, and 353, while the blue symbols to DIRBE 140, 240, *Planck* 217, and 143, not used to constrain the fit. The solid black line to the total DL SED, while the green solid line correspond to its PDR component and the blue solid line to the diffuse cloud component. In each band we show the percentual deviation of the model from the observed flux.

7. Variation in optical extinction to FIR emission in dense areas: molecular clouds

In Sect. 6 we presented an analysis of the DL optical performance in the diffuse sky, comparing its A_V estimates with those derived from a QSO sample. We now extend the analysis to molecular clouds. We further study the dependence of the optimal renormalization as a function of the remaining relevant fitted parameter: $\Sigma_{M_{\rm d}}$. We present the extinction maps based on stellar observations on Sect. 7.1. We compare the DL and stellar extinction maps on Sect. 7.2. We finally discuss a model renormalization for molecular clouds in Sect. 7.3.

7.1. Extinction maps of molecular clouds

Schneider et al. (2011) presented optical extinction maps, noted $A_{V,\rm 2M}$, of several clouds computed using stellar observations from the 2MASS catalogue in the J, H, and K bands. We now compare these $A_{V,\rm 2M}$ maps with the DL estimates generated by modelling the dust FIR emission, $A_{V,\rm DL}$. The Schneider et al. (2011) A_V maps were computed using a 2′ Gaussian PSF, and we degrade them to a 5′ Gaussian PSF to perform our analysis. We use the maps of the Cepheus, Chamaeleon, Ophiuchus, Orion, and Taurus cloud complexes.

The 2MASS maps were corrected for a zero level offset (adding an inclined plane) using an algorithm similar to

that adopted to estimate the background in the analysis of the KINGFISH sample of galaxies, described in AD12. The algorithm iteratively and simultaneously matches the zero level and inclination of the $A_{V,\mathrm{RQ}}$ and $A_{V,\mathrm{2M}}$ maps, as well as estimating the areas that are considered background.

Figure 13 shows the 2MASS $A_{V,\mathrm{2M}}$ map, the DL U_{min} map, the DL $A_{V,\mathrm{DL}}$ map (divided by 2.95, see Sect. 7.2) and the renormalized $A_{V,\mathrm{RQ}}$ map for the Chamaeleon region. The inner (high A_V) areas correspond to lower U_{min} values, as the heating radiation field gets extincted when penetrating into the dense cloud. The remaining cloud complexes show similar $A_V - U_{\mathrm{min}}$ behaviour.

7.2. 2MASS – DL optical extinction comparison in molecular clouds

For each cloud we find an approximate linear relation between the $A_{V,\mathrm{2M}}$ map and the $A_{V,\mathrm{DL}}$ map. However, as in the case of the diffuse ISM, the (FIR based) $A_{V,\mathrm{DL}}$ estimates are significantly larger than the (optical) $A_{V,\mathrm{2M}}$ estimates. For the selected clouds, the DL model overestimates the 2MASS stellar A_V by factors of 2 – 3. Table 3 provides the multiplicative factors needed to make the DL A_V maps agree with the 2MASS A_V maps.

Table 3. Mean ratio between the DL and 2MASS extinction estimates in molecular clouds.

Cloud name	$A_{V,\mathrm{DL}}$ versus $A_{V,\mathrm{2M}}$ slope[a]
Cepheus	2.67
Chamaeleon	2.95
Ophiuchus	2.19
Orion	2.73
Taurus	2.86

a Note that the $A_{V,\mathrm{RQ}}$ versus $A_{V,\mathrm{2M}}$ slope is very close to 1.0, the renormalized DL estimate predicts the 2MASS A_V accurately in most pixels.

Figure 14 shows the comparison of the DL maps and the 2MASS maps in the Chamaeleon cloud. The left panel shows the $A_{V,\mathrm{DL}}$ versus $A_{V,\mathrm{2M}}$ values, and the right panel the renormalized $A_{V,\mathrm{RQ}}$ versus $A_{V,\mathrm{2M}}$ values. After multiplicative adjustment, the $A_{V,\mathrm{DL}}$ and $A_{V,\mathrm{2M}}$ estimates agree reasonably well over the entire cloud complex. The low surface brightness areas are sensitive to background level mismatch. The renormalization presented in Section 6.3, computed in diffuse ($A_V < 1$, although most of the QSO have $A_V \approx 0.1$) regions, actually brings the $A_{V,\mathrm{DL}}$ and $A_{V,\mathrm{2M}}$ estimates into better agreement in the molecular clouds than the re-scaled $A_{V,\mathrm{DL}}$.

Figure 15 shows the comparison of the renormalized $A_{V,\mathrm{RQ}}$ maps and the $A_{V,\mathrm{2M}}$ maps in all the clouds. The model renormalization was originally computed to bring into agreement the DL and QSO A_V estimates in the diffuse ISM. The renormalization also accounts quite well (within 10 %) for the discrepancies between 2MASS and DL A_V estimates in molecular clouds in the $0 < A_V < 3$ range, and even does passably well (within 30 %) up to $A_V \approx 8$.

7.3. Dependence of the DL A_V overestimation on U_{min} in molecular clouds.

In the diffuse ISM analysis, we concluded that U_{min} is actually simultaneously tracing variations in the radiation field heating the dust, and in the dust opacity. One could expect that both phenomena are also present in other environments, e.g., molecular clouds, but their relative contribution in determining the SED peak (and therefore U_{min}) need not be the same as in the diffuse ISM. Therefore, a renormalization of the DL A_V based on 2MASS data should, in principle, be different from that determined using the QSOs.

Figure 16 compares the DL and 2MASS A_V estimates. It is analogous to Figure 9, but using the 2MASS A_V estimates $A_{V,\mathrm{2M}}$ instead of those from QSOs. It shows the ratio $A_{V,\mathrm{DL}}$ / $A_{V,\mathrm{2M}}$, as a function of the fitted U_{min}. This includes the pixels from the five cloud complexes with $1 < \mathrm{2MASS}\, A_V < 5$. For each U_{min} value, the solid curve correspond to the best fit slope of the $A_{V,\mathrm{DL}}$ versus $A_{V,\mathrm{2M}}$ values (i.e., it is an estimate of a weighted mean of the $A_{V,\mathrm{DL}}$ / $A_{V,\mathrm{2M}}$ ratio). The straight solid line correspond to a fit to the solid curve in the $0.2 < U_{\mathrm{min}} < 1.0$ range. In this fit, each U_{min} is given a weight proportional to the number pixels that have this value in the clouds (i.e., most of the weight is for the pixels within the $0.2 < U_{\mathrm{min}} < 0.8$ range. The dashed line correspond to the renormalization proposed in Sect. 6.3 (Eq. 9) that brings into agreement the $A_{V,\mathrm{DL}}$ estimates with the QSOs $A_{V,\mathrm{QSO}}$.

The straight line in Figure 16 correspond to a renormalization tailored to bring into agreement the $A_{V,\mathrm{DL}}$ and $A_{V,\mathrm{2M}}$ estimates, i.e., a "2MASS" renormalization for molecular the clouds, noted $A_{V,\mathrm{RC}}$. The 2MASS renormalization is given by

$$A_{V,\mathrm{RC}} = (0.33\, U_{\mathrm{min}} + 0.27) \times A_{V,\mathrm{DL}}. \quad (10)$$

Empirically, $A_{V,\mathrm{RC}}$ is our best estimator of the 2MASS extinction $A_{V,\mathrm{2M}}$. Surprisingly, the 2MASS normalization $A_{V,\mathrm{RC}}$ for molecular clouds is quite close to the QSO normalization $A_{V,\mathrm{QSO}}$.

8. Discusion

The DL A_V estimates, based on the dust FIR emission, differ significantly from estimates based on optical observations. We describe this discrepancy and discuss possible origins in Sect. 8.1. With the aim of obtaining a more accurate A_V map, we empirically correct the DL A_V estimate in Sect. 8.2.

8.1. DL FIR emission and optical extinction disagreement

In the diffuse ISM, the DL, at first sight, provide good fits to the Galactic SED as observed by *WISE*, *IRAS*, and *Planck*, as it has been the case in the past for external galaxies observed with *Spitzer* and *Herschel*. However, the fit is not fully satisfactory, because the optical extinction from the model does not agree with the observed extinction toward QSOs and molecular clouds. The optical extinction disagreement can be decomposed in two levels:

- a basic disagreement, which corresponds to the mean factor of 1.9 between the DL and QSOs A_V values;
- a secondary disagreement, which is expressed in the dependence of the ratios between the DL and QSO A_V values on U_{min}.

The result of the SED fit depends on the spectral shape of the dust opacity. The DL model spectral shape departs slightly

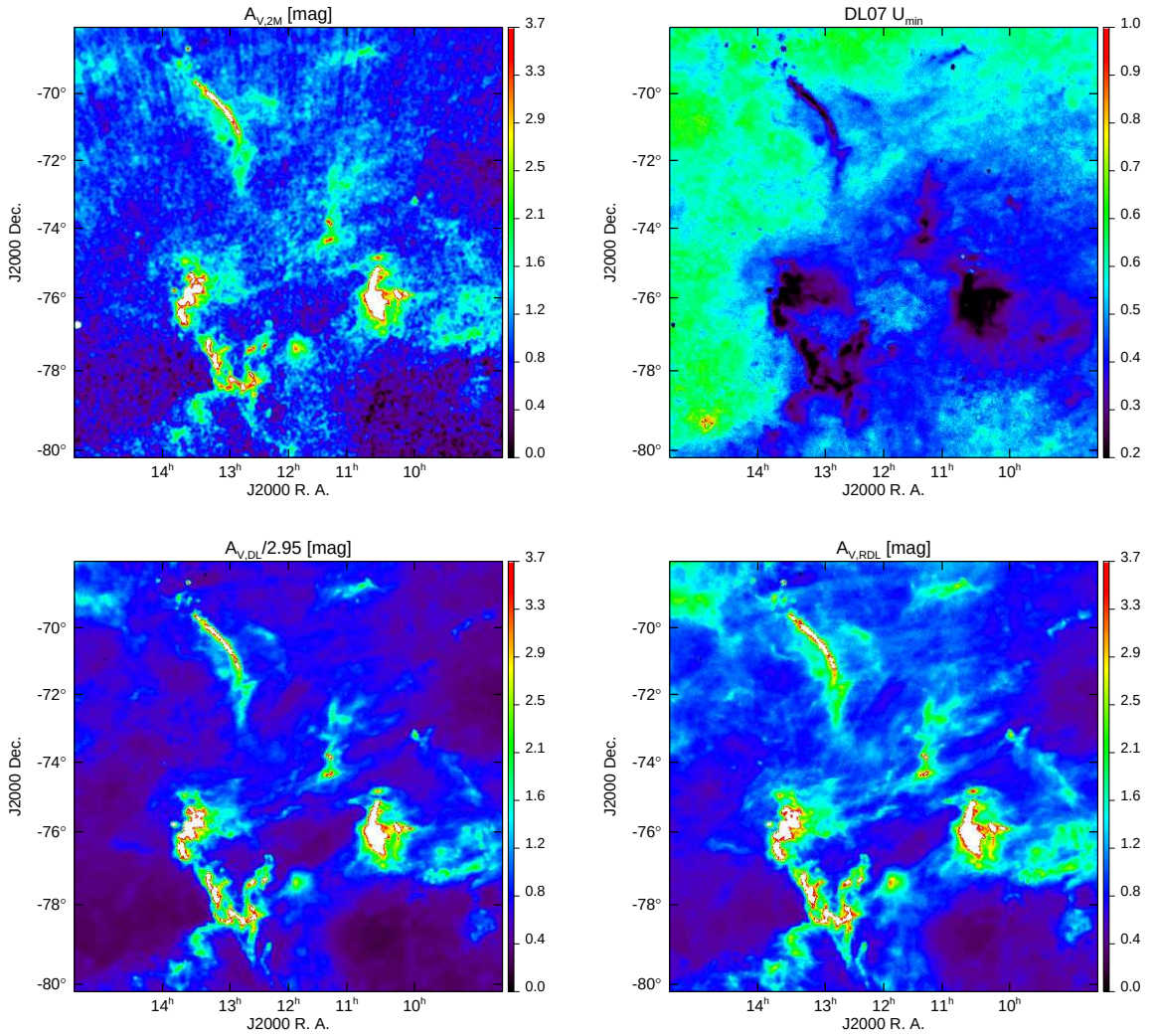

Fig. 13. 2MASS and DL estimates in the Chamaeleon cloud region. The top row shows the (background corrected) 2MASS $A_{V,2M}$ map (left) and the DL $U_{\rm min}$ map (right). The bottom row shows the DL $A_{V,DL}$ estimate divided by 2.95 (left), and the renormalized model $A_{V,RQ}$ estimates (right). (See Sect. 7.2 for a derivation of the 2.95 factor)

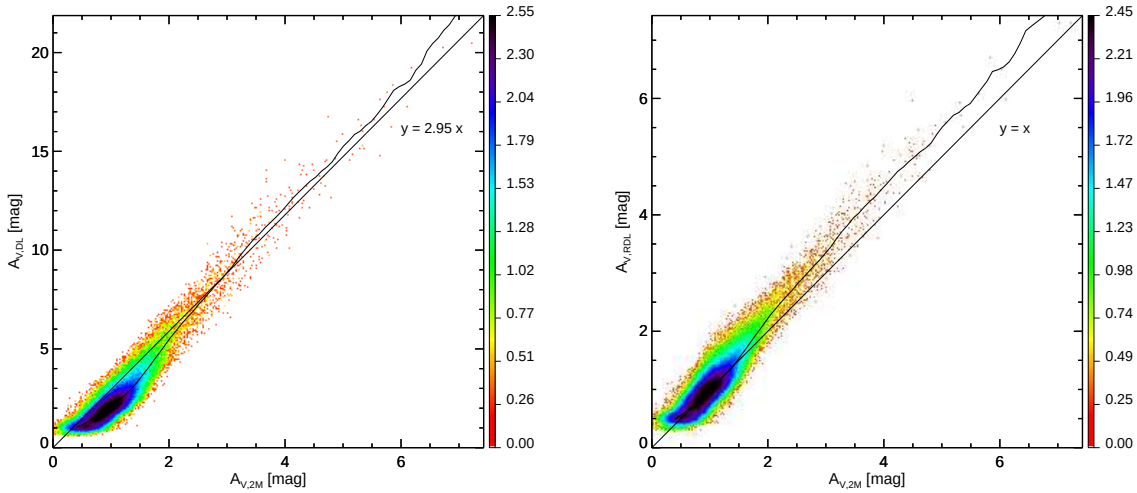

Fig. 14. 2MASS and DL A_V comparison in the Chamaeleon cloud. The left panel shows the $A_{V,DL}$ versus $A_{V,2M}$ values, and the right panel the renormalized $A_{V,RQ}$ versus $A_{V,2M}$ values. The diagonal lines correspond to $y = 2.95x$, and $y = x$ respectively, and the curves correspond to the mean value.

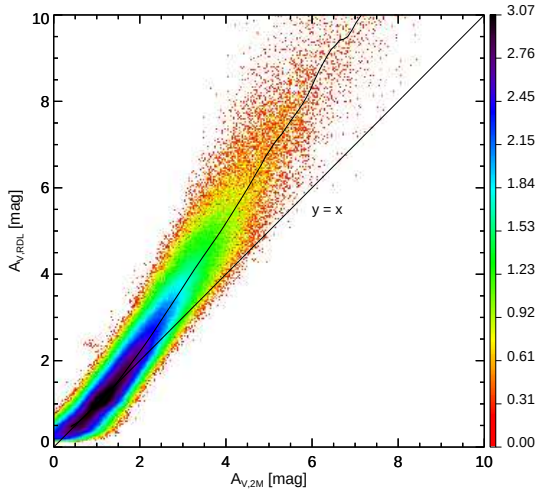

Fig. 15. Comparison of the renormalized $A_{V,\mathrm{RQ}}$ and 2MASS $A_{V,2\mathrm{M}}$ estimates. The individual pixels of the Cepheus, Chamaeleon, Ophiuchus, Orion, and Taurus clouds are combined. Colour corresponds to the logarithm of the density of points (see Figure 5). The diagonal line correspond to $y = x$, and the curve correspond to the mean value.

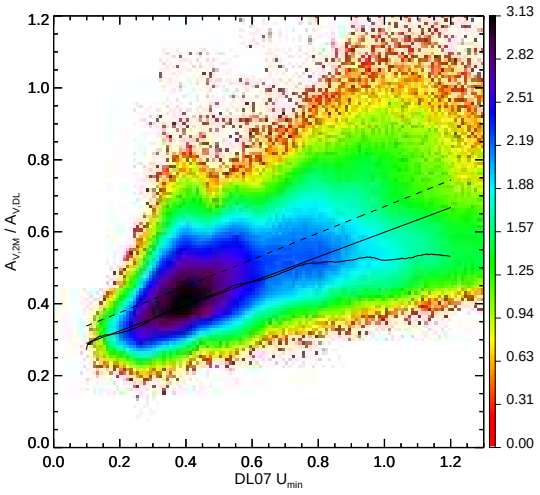

Fig. 16. Renormalization of the DL A_V values in molecular clouds. Pixels from the five molecular complexes with $1 < A_V < 5$ are included here. Colour corresponds to the logarithm of the density of points (see Figure 5). For each U_{min} value, the solid curve correspond to the best fit slope of the $A_{V,\mathrm{DL}}$ versus $A_{V,2\mathrm{M}}$ values. The straight solid line correspond to a fit to the solid curve in the $0.2 < U_{\mathrm{min}} < 1.0$ range, where each U_{min} is given a weight proportional to the number pixels that have this value in the clouds. The straight solid line provides the $A_{V,\mathrm{RC}}$ renormalization (Eq. 10) . The dashed line correspond to the renormalization found in the QSO analysis (Eq. 9), i.e., the line that provides the $A_{V,\mathrm{RQ}}$ renormalization (represented as a solid line in Figure 9).

from that of the *Planck* 857, 545, and 353 data in the diffuse ISM (shown by Figure 12). This makes the DL model fit with a lower U_{min} value than the true radiation field intensity, which turns into an increase of the A_V estimates [18]. This global disagreement could also be indicating that the DL dust material has a FIR–submm opacity per unit of optical extinction that is too low. Other dust models with different (but fixed) optical properties may show a different global factor, possibly closer to 1.

The second issue shows that variations in the FIR–submm opacity, in its normalization per unit of optical extinction, or the spectral shape, are needed across the sky; we take this to be evidence of dust evolution. This discrepancy will be present for all dust models based on fixed dust optical properties, possibly with a different magnitude depending of the details of the specific model.

8.2. Optical exctinction A_V estimates of dust models

With the aim of obtaining an accurate A_V map of the sky, we proposed the renormalized DL A_V estimates ($A_{V,\mathrm{RQ}}$ in Eqs. 9 and $A_{V,\mathrm{RC}}$ in 10) that compensates for the discrepancy between the observed FIR emission and the optical extinction in the directions of QSOs and molecular clouds. Essentially, it rescales one of the model outputs (the dust optical extinction A_V) by a function of U_{min}, to match data. Planck Collaboration Int. XIV (2013) presented an independent comparison of the renormalized $A_{V,\mathrm{RQ}}$ estimates with $\gamma-$ray observations in the Chamaeleon cloud. They concluded that the "renormalized" $A_{V,\mathrm{RQ}}$ estimates are in closer agreement with $\gamma-$ray A_V estimates than the (non-renormalized) $A_{V,\mathrm{DL}}$ estimates. We now discuss the model renormalization in a more general context.

The renormalized DL estimates ($A_{V,\mathrm{RQ}}$ and $A_{V,\mathrm{RC}}$) provide a good A_V determination in the areas where they were calibrated, but they do not provide any insight into the physical dust properties per se; the renormalized dust model becomes simply a family of SEDs used to fit the data, from which we construct and calibrate an observable quantity ($A_{V,\mathrm{RQ}}$ and $A_{V,\mathrm{RC}}$). Unfortunately, the fitted parameters of the renormalized model (U_{min}) lack a physical interpretation: U_{min} is not solely tracing the heating intensity of the radiation field, as was assumed in DL.

The A_V estimate of the DL dust model is a function of its fitted parameters, i.e., $A_V = f(\Sigma_{M_\mathrm{d}}, q_{\mathrm{PAH}}, \gamma, U_{\mathrm{min}})$. In general, if we fit a dust model with several parameters, A_V will be a function of the "most relevant" parameters[19]. The DL model assumes $A_V = f(\Sigma_{M_\mathrm{d}}) = k \times \Sigma_{M_\mathrm{d}}$, with $k = 0.74 \times 10^{-5}\,\mathrm{mag\,M_\odot^{-1}\,kpc^2}$. Our proposed renormalizations are a first step toward a "functional renormalization" by extending $A_V = k \times \Sigma_{M_\mathrm{d}}$ into $A_V = g(U_{\mathrm{min}}) \times k \times \Sigma_{M_\mathrm{d}}$, where we take $g(U_{\mathrm{min}})$ to be a linear function of U_{min}. Due to the larger scatter in the QSO A_V estimates, only a simple linear function $g(U_{\mathrm{min}})$ can be robustly estimated in the diffuse ISM. In molecular clouds, where the data are less noisy, one could find a smooth function $g'(U_{\mathrm{min}})$ which better matches the $A_{V,\mathrm{DL}}$ / $A_{V,2\mathrm{M}}$ fit for each U_{min} (i.e., in Figure 16, the solid curve "flattens" for $U_{\mathrm{min}} > 0.8$, departing from its linear fit).

Unfortunately any renormalization procedure, while leading to a more accurate A_V estimate, does not provide any further insight into the dust physical properties. Real physical knowledge will arise from a new generation of dust models that should be able to predict the correct optical extinction A_V from first principles. The next generation of dust models should be able to fit the empirical SEDs presented in Sect. 6.4 directly. While such a new generation of dust models is not yet available, we can for now correct for the systematic departures via Eqs. 9 and 10 in the diffuse and dense regions, respectively.

[18] For example, if an MBB with T = 19K, $\beta = 1.9$ is fitted with an MBB with $\beta = 1.8$, using the *IRAS* 100, *Planck* 857, *Planck* 545, and *Planck* 353 bands, then the fitted amplitude will be 30 % larger than the original one. Therefore, a discrepancy of $\delta\Upsilon = 0.1$ is likely to produce a bias in the A_V estimates of the order of 30 %.

[19] In the MBB approach, one should consider a function of the form $A_V = f(\tau_{353}, T, \beta)$.

9. Conclusions

We present a full-sky dust modelling of the new *Planck* data, combined with ancillary *IRAS* and *WISE* data, using the DL dust model. We test the model by comparing these maps with independent estimates of the dust optical extinction A_V using SDSS QSO photometry and 2MASS stellar data. Our analysis provides new insight on interstellar dust and a new A_V map over the full sky.

The DL model fits the observed *Planck*, *IRAS*, and *WISE* SEDs well over most of the sky. Moreover, in the diffuse ISM the DL model fits the observed SED in the *Planck* 857 – *Planck* 143 range satisfactorily. The modelling is robust against changes in the angular resolution, as well as adding DIRBE 140 and DIRBE 240 photometric constraints. The high resolution parameter maps that we generated trace the Galactic dusty structures well, using a state-of-the-art dust model. We produced the best possible optical extinction A_V maps using the DL model.

In the diffuse ISM, the DL A_V estimates are larger than estimates from QSO optical photometry by approximately a factor of 2, and this discrepancy depends systematically on $U_{\rm min}$. In molecular clouds, the DL A_V estimates are larger than estimates based on 2MASS stellar photometry by a factor of about 3. Again, the discrepancy depends in a similar way on $U_{\rm min}$.

We conclude that the current parameter $U_{\rm min}$, associated with the peak wavelength of the SED, does not only trace variations in the intensity of the radiation field heating the dust. $U_{\rm min}$ also traces dust evolution: i.e., variations in the optical and FIR properties of the dust grains in the diffuse ISM. DL is a physical dust model. Physical dust models have the advantage that, if successful, they give some support to the physical assumptions made about the interstellar dust and ISM properties that they are based on. Unfortunately, the discrepancies found in this study indicate that some of the physical assumptions of the model need to be revised.

We provide a one-parameter family of SEDs per unit of dust optical extinction in the diffuse ISM. These SEDs, which relate the dust emission and absorption properties, are independent of the dust/gas ratio or problems inferring total H column density from observations. The next generation of dust models will need to reproduce these new SED estimates.

We propose an empirical renormalization of the DL A_V values as a function of the DL $U_{\rm min}$ parameter. The renormalized DL A_V estimates trace the QSO A_V estimates. The proposed renormalization ($A_{V,\rm RQ}$), derived in the diffuse ISM, also brings into agreement the DL A_V estimates with those derived from 2MASS optical photometry toward molecular clouds in the $0 < A_V < 5$ range. We propose a second renormalized DL A_V estimate ($A_{V,\rm RC}$) tailored to trace the A_V estimates in molecular clouds more precisely, (and see also the comparison with Fermi γ – rays data in Planck Collaboration Int. XIV (2013)). The renormalized map $A_{V,\rm RQ}$ is the most accurate estimate of the optical extinction in the diffuse ISM based on our QSOs analysis. Comparison of the $A_{V,\rm RQ}$ map against other tracers of interstellar extinction, probing different environment, would further test its accuracy and check for any potential systematics in the QSO analysis.

Acknowledgements. The development of *Planck* has been supported by: ESA; CNES and CNRS/INSU-IN2P3-INP (France); ASI, CNR, and INAF (Italy); NASA and DoE (USA); STFC and UKSA (UK); CSIC, MICINN, JA, and RES (Spain); Tekes, AoF, and CSC (Finland); DLR and MPG (Germany); CSA (Canada); DTU Space (Denmark); SER/SSO (Switzerland); RCN (Norway); SFI (Ireland); FCT/MCTES (Portugal); and PRACE (EU). A description of the Planck Collaboration and a list of its members, including the technical or scientific activities in which they have been involved, can be found at `http://www.sciops.esa.int/index.php?project=planck&page=Planck_Collaboration`.

The research leading to these results has received funding from the European Research Council under the European Union's Seventh Framework Programme (FP7/2007-2013) / ERC grant agreement n 267934.

References

Abazajian, K. N., Adelman-McCarthy, J. K., Agüeros, M. A., et al. 2009, ApJS, 182, 543
Aniano, G., Draine, B. T., Calzetti, D., et al. 2012, ApJ, 756, 46
Aniano, G., Draine, B. T., Calzetti, D., et al. 2014, in preparation
Boggess, N. W., Mather, J. C., Weiss, R., et al. 1992, ApJ, 397, 420
Bohlin, R. C., Savage, B. D., & Drake, J. F. 1978, ApJ, 224, 132
Boselli, A., Eales, S., Cortese, L., et al. 2010, PASP, 122, 261
Ciesla, L., Boquien, M., Boselli, A., et al. 2014, A&A, 565, A128
Compiègne, M., Verstraete, L., Jones, A., et al. 2011, A&A, 525, A103
de Vaucouleurs, G., de Vaucouleurs, A., Corwin, Jr., H. G., et al. 1991, Third Reference Catalogue of Bright Galaxies (New York: Springer)
Desert, F.-X., Boulanger, F., & Puget, J. L. 1990, A&A, 237, 215
Draine, B. T., Aniano, G., Krause, O., et al. 2014, ApJ, 780, 172
Draine, B. T., Dale, D. A., Bendo, G., et al. 2007, ApJ, 663, 866
Draine, B. T. & Hensley, B. 2012, ApJ, 757, 103
Draine, B. T. & Lee, H. M. 1984, ApJ, 285, 89
Draine, B. T. & Li, A. 2007, ApJ, 657, 810
Dwek, E. 1998, ApJ, 501, 643
Fazio, G. G., Hora, J. L., Allen, L. E., et al. 2004, ApJS, 154, 10
Finkbeiner, D. P., Davis, M., & Schlegel, D. J. 1999, ApJ, 524, 867
Fitzpatrick, E. L. 1999, PASP, 111, 63
Górski, K. M., Hivon, E., Banday, A. J., et al. 2005, ApJ, 622, 759
Griffin, M. J., Abergel, A., Abreu, A., et al. 2010, A&A, 518, L3
Jones, A. P., Fanciullo, L., Köhler, M., et al. 2013, A&A, 558, 62
Kalberla, P. M. W., Burton, W. B., Hartmann, D., et al. 2005, A&A, 440, 775
Kawada, M., Baba, H., Barthel, P. D., et al. 2007, PASJ, 59, 389
Kelsall, T., Weiland, J. L., Franz, B. A., et al. 1998, ApJ, 508, 44
Kennicutt, R. C., Armus, L., Bendo, G., et al. 2003, PASP, 115, 928
Li, A. & Draine, B. T. 2001, ApJ, 554, 778
Liszt, H. 2014a, ApJ, 783, 17
Liszt, H. 2014b, ApJ, 780, 10
Mathis, J. S., Mezger, P. G., & Panagia, N. 1983, A&A, 128, 212
Meisner, A. M. & Finkbeiner, D. P. 2014, ApJ, 781, 5
Miville-Deschênes, M.-A. & Lagache, G. 2005, ApJS, 157, 302
Murakami, H., Baba, H., Barthel, P., et al. 2007, PASJ, 59, 369
Neugebauer, G., Habing, H. J., van Duinen, R., et al. 1984, ApJ, 278, L1
Pâris, I., Petitjean, P., Aubourg, É., et al. 2013, ArXiv e-prints
Pascale, E., Ade, P. A. R., Bock, J. J., et al. 2008, ApJ, 681, 400
Pilbratt, G. L., Riedinger, J. R., Passvogel, T., et al. 2010, A&A, 518, L1
Planck Collaboration XVII. 2011, A&A, 536, A17
Planck Collaboration XXIV. 2011, A&A, 536, A24
Planck Collaboration I. 2014, A&A, in press, arXiv:1303.5062
Planck Collaboration VIII. 2014, A&A, in press, arXiv:1303.5069
Planck Collaboration XI. 2014, A&A, in press, arXiv:1312.1300
Planck Collaboration XII. 2014, A&A, in press, arXiv:1303.5072
Planck Collaboration XIV. 2014, A&A, in press, arXiv:1303.5074
Planck Collaboration Int. XIV. 2013, Planck intermediate results. XXVIII. A dust and gas census in the Gould Belt clouds with Planck and Fermi (Submitted to A&A, [arXiv:astro-ph/1303.xxxx])
Planck Collaboration Int. XVII. 2014, A&A, 566, A55
Planck Collaboration Int. XXV. 2014, A&A, submitted, arXiv:1407.5452
Poglitsch, A., Waelkens, C., Geis, N., et al. 2010, A&A, 518, L2
Rieke, G. H., Young, E. T., Engelbracht, C. W., et al. 2004, ApJS, 154, 25
Schlegel, D. J., Finkbeiner, D. P., & Davis, M. 1998, ApJ, 500, 525
Schneider, N., Bontemps, S., Simon, R., et al. 2011, A&A, 529, A1
Siebenmorgen, R., Voshchinnikov, N. V., & Bagnulo, S. 2014, A&A, 561, A82
Silverberg, R. F., Hauser, M. G., Boggess, N. W., et al. 1993, SPIE, 2019, 180
Skrutskie, M. F., Cutri, R. M., Stiening, R., et al. 2006, AJ, 131, 1163
Vanden Berk, D. E., Richards, G. T., Bauer, A., et al. 2001, AJ, 122, 549
Vilardell, F., Ribas, I., Jordi, C., Fitzpatrick, E. L., & Guinan, E. F. 2010, A&A, 509, A70
Weingartner, J. C. & Draine, B. T. 2001, ApJ, 548, 296
Werner, M. W., Roellig, T. L., Low, F. J., et al. 2004, ApJS, 154, 1
Wiebe, D. V., Ade, P. A. R., Bock, J. J., et al. 2009, ApJ, 707, 1809
Wright, E. L., Eisenhardt, P. R. M., Mainzer, A. K., et al. 2010, AJ, 140, 1868
York, D. G., Adelman, J., John E. Anderson, J., et al. 2000, ApJ, 120, 1579
Zubko, V., Dwek, E., & Arendt, R. G. 2004, ApJS, 152, 211

Appendix A: Comparison with *Spitzer* + *Herschel* modelling of the Andromeda galaxy

The Andromeda galaxy is the nearest large spiral galaxy. It provides a useful benchmark to validate the current dust modelling. Its isophotal radius is $R_{25} = 95'$ (de Vaucouleurs et al. 1991), corresponding to $R_{25} = 20.6$ kpc at the assumed distance $d = 744$ kpc (Vilardell et al. 2010).

Several authors have modelled the dust properties of M31. Planck Collaboration Int. XXV (2014) presented an independent study to M31 using *Planck* maps and MBB dust model. In particular DA14 presented a DL based modelling of M31 using the IRAC (Fazio et al. 2004) and MIPS (Rieke et al. 2004) instruments on *Spitzer*, and the PACS (Poglitsch et al. 2010) and SPIRE (Griffin et al. 2010) instruments on *Herschel*. This data set has 13 photometric constraints (IRAC 3.6 μm, 4.5 μm, 5.8 μm, and 8.0 μm, MIPS 24 μm, 70 μm, and 160 μm, PACS 70 μm, 100 μm, and 160 μm, and SPIRE 250 μm, 350 μm, and 500 μm) from a different set of instruments than those used in our analysis. The high resolution modelling traces the structures of M31 in great detail, providing maps of $U_{\rm min}$ and dust surface density, and enables a comparison to be made with gas and metallicity observations. The modelling techniques are described and validated on NGC628 and NGC6946 in AD12, and later expanded to the full KINGFISH galaxy sample in AD13.

We compare the dust mass surface density maps[20] of the modelling presented by DA14 (from now on called "*Herschel*") degraded to a 5′ Gaussian PSF, with the current modelling, called "*Planck*". In the *Herschel* modelling, a tilted plane is fitted to the background areas, and subtracted from the original images to remove the Milky Way cirrus emission. Therefore, we need to add the cirrus emission back to the *Herschel* mass estimates before comparing to the *Planck* modelling. The zero level of the *Herschel* modelling was restored with an algorithm similar to that used to estimate the background planes in the KINGFISH dust modelling (see AD12). This algorithm iteratively fits an inclined plane to the difference in mass surface densities over the background points.

M31 does not have considerable quantities of cold dust, which would be detected in the *Planck* modelling but not in the *Herschel* modelling. Therefore, we expect both modellings to agree well.

Figure A.1 presents the comparison of the two dust models. The "*Herschel*" and "*Planck*" approaches agree very well: the resolved mass differences between the two analyses is small, only 10 % across most of the galaxy. The remaining parameter estimates also agree well. In conclusion, the model results appear not to be sensitive to the specific data sets used to constrain the FIR dust emission. This comparison validates the present modelling pipeline and methodology.

PIP52 (the reference is still not in the Planck.bib file, I will update this as soon as it becomes available) presented an independent MBB modelling of M31 using the sample *Planck* data as the current analysis, and found compatible results with our DL modelling.

Appendix B: QSO A_V estimation

The intrinsic colours of an unobscured QSO depend strongly on its redshift[21] (ζ). We first estimate the (redshift dependent) unobscured QSO colour for each band pair. By comparing each QSO colours with the expected unobscured colours, we can estimate its reddening. Assuming a typical dust extinction curve, we can combine the reddening estimates of the band pairs into a single extinction estimate for each QSO. This analysis relies on the fact that the mean colour excess of a group of QSO scales linearly with the DL A_V estimates (see Figure B.2).

B.1. SDSS QSO catalogue

The SDSS is a photometric and spectroscopic survey, using a dedicated 2.5-m telescope at Apache Point Observatory in New Mexico. It has produced high quality observations of approximately 10^4 deg^2 of the northern sky in five optical and near IR bands: *u*, *g*, *r*, *i*, and *z*, centred at 354.3 nm, 477.0 nm, 623.1 nm, 762.5 nm, and 913.4 nm respectively (York et al. 2000). The SDSS seventh data release (DR7) (Abazajian et al. 2009) contains a sample of 105 783 spectroscopically confirmed QSOs,and the SDSS tenth data release (DR10) (Pâris et al. 2013) contains an additional sample of 166 583 QSOs.

In order to avoid absorption from the intergalactic medium, each SDSS band is only usable up to the redshift at which the Lyα line (121.57 nm vacuum wavelength) enters (from the blue side) into the filter. Therefore, we can use the *u*-band, for QSOs with $\zeta < 1.64$, *g*-band for $\zeta < 2.31$, *r*-band for $\zeta < 3.55$, *i*-band for $\zeta < 4.62$, and *z*-band for $\zeta < 5.69$. We also limit the study to $0.35 < \zeta < 3.35$, to have enough QSOs per unit of redshift to estimate reliably the redshift-dependent unobscured QSO intrinsic colour (see Sect. B.2). We also remove the few QSOs that lie in very luminous ($L_{\rm dust} > 10^8 L_\odot$ kpc^{-2}), very massive ($A_V > 1$), very hot ($U_{\rm min} > 1.2$) or very cold ($U_{\rm min} < 0.3$) lines of sight. This leaves 261 841 useful QSOs.

B.2. Unobscured QSO intrinsic colours and extinction estimation

A typical QSO spectrum has several emission and absorption lines superimposed on a power-law-like continuum. Depending on the QSO redshift, the lines fall in different filters. Therefore, for each optical band pair (X, Y), the unobscured QSO intrinsic colour $C_{X,Y}(\zeta)$ depends on the QSO redshift. Given two photometric bands X and Y, in order to estimate the unobscured QSO intrinsic colour $C_{X,Y}(\zeta)$, we proceed as follows.

We will see that the intrinsic dust properties appear to depend on the parameter $U_{\rm min}$. Therefore, to avoid introducing a potential bias when computing $C_{X,Y}(\zeta)$, we group the lines of sight according to $U_{\rm min}$, and analyze each group independently. The functions $C_{X,Y}(\zeta)$ should, in principle, not depend on $U_{\rm min}$, and therefore, all the estimates $C_{X,Y}(\zeta, U_{\rm min})$ should be similar for the different $U_{\rm min}$ sets. Working independently on each $U_{\rm min}$, for each redshift ζ we choose all the QSOs in the interval $[\zeta - 0.05, \zeta + 0.05]$, or the 2000 closest QSOs if there are more than 2000 QSOs in the interval, and fit the QSOs colour $(X - Y)$ as a function of the dust column density:

$$(X - Y) = C_{X,Y}(\zeta, U_{\rm min}) + \eta_{X,Y}(\zeta, U_{\rm min}) \times A_{V,\rm DL}, \qquad \text{(B.1)}$$

where $A_{V,\rm DL}$ is the DL estimated dust extinction in each QSO line of sight. The function $C_{X,Y}(\zeta, U_{\rm min})$ is the best estimate of the colour difference $(X - Y)$ of an unobscured QSO ($A_{V,\rm DL} = 0$) at redshift ζ, estimated from the lines of sight of dust fitted with $U_{\rm min}$. The function $\eta_{X,Y}(\zeta, U_{\rm min})$ should be essentially indepen-

[20] Both dust mass surface density maps correspond to the line of sight projected densities, not corrected for the M31 inclination.

[21] We will denote the QSO redshift as ζ, instead of the usual z to avoid confusion with the longest wavelength SDSS filter *z*.

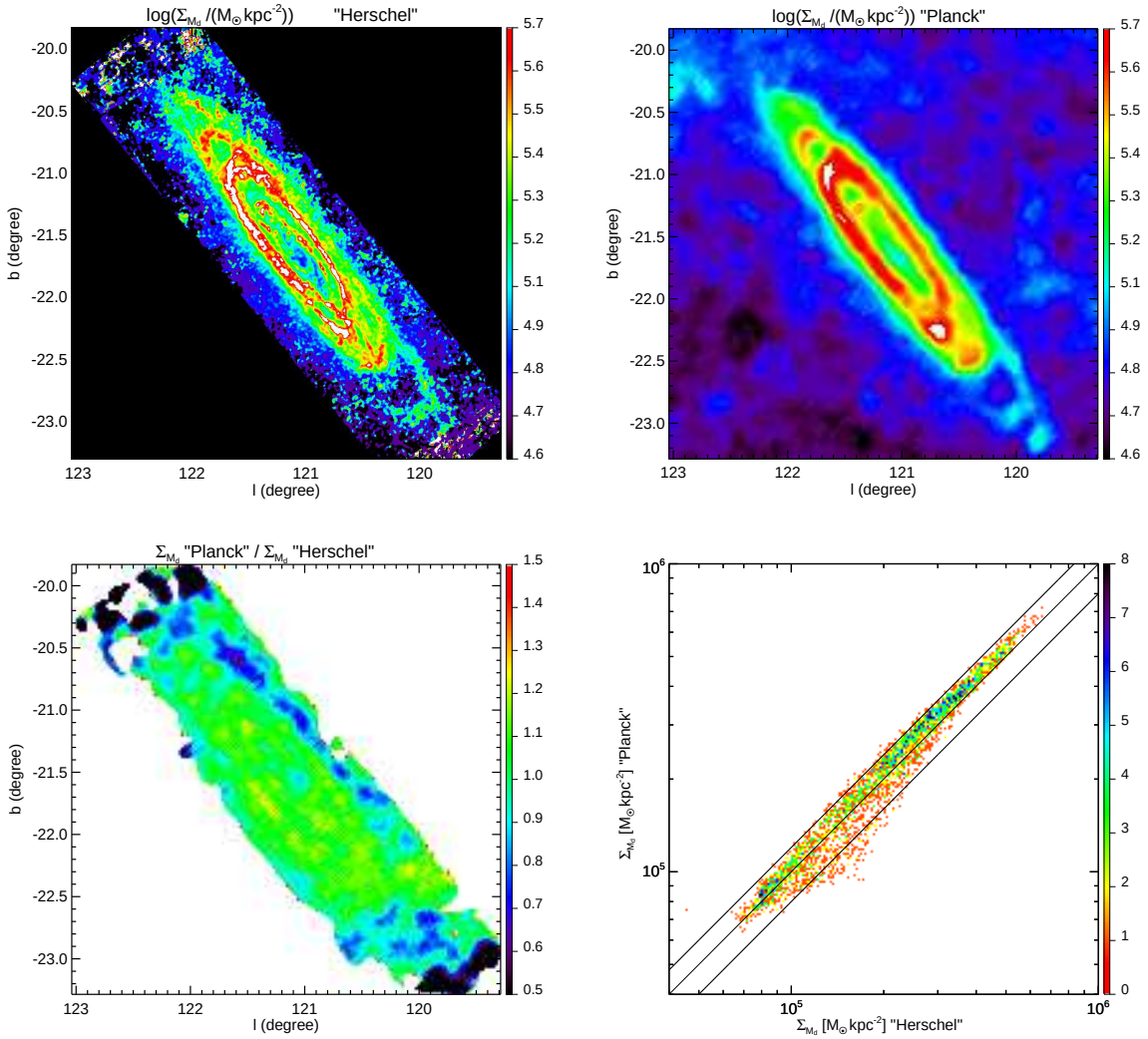

Fig. A.1. Comparison of M31 maps as seen by *Herschel* and *Planck*. The top row shows maps of the dust mass generated using *Spitzer* and *Herschel* data at high resolution (left) and the current estimates using *IRAS* and *Planck* data (right). The bottom row shows the ratio map of the two mass estimates (convolved to a common resolution and with the zero level matched) on the left, and their scatter on the right. The diagonal lines in the bottom right panel, correspond to a one-to-one relationship, and a ±20 % difference about that. The colour in the last panel corresponds to the density of points. Even though the two analyses are based on completely independent data, they agree remarkably well, differing by less than 10 % across most of the galaxy.

dent of ζ[22]. Variations in the function $\eta_{X,Y}(\zeta, U_{\rm min})$ with respect to $U_{\rm min}$ give us information about the dust properties.

Once we compute $C_{X,Y}(\zeta, U_{\rm min})$ for the different values of $U_{\rm min}$, we average them for each redshift ζ to obtain $C_{X,Y}(\zeta)$. For each $U_{\rm min}$ and ζ, the weight given to each $C_{X,Y}(\zeta, U_{\rm min})$ value is proportional to the number of QSO in the $[\zeta - 0.05, \zeta + 0.05]$ interval. Figure B.1 shows the results of this unobscured QSO intrinsic colour estimation algorithm for the bands i and z. The functions $C_{i,z}(\zeta, U_{\rm min})$ are shown for the different values of $U_{\rm min}$, using redder lines for larger $U_{\rm min}$, and greener for smaller $U_{\rm min}$. Their weighted mean $C_{i,z}(\zeta)$ is shown in black.

For each QSO, we define its reddening $E_{X,Y}$ as:

$$E_{X,Y} = (X - Y) - C_{X,Y}(\zeta). \quad \text{(B.2)}$$

The $E_{X,Y}$ values should not depend on the redshift, and therefore we can group all the QSOs of a given $U_{\rm min}$ into a sub sample with the same intrinsic colour. Note that no additional hypotheses on the QSO spectral shape or dust extinction curve need to be made to compute the QSO intrinsic colours. Working with all the QSOs with a given $U_{\rm min}$, we fit

$$E_{X,Y} = \eta_{X,Y}(U_{\rm min}) \times A_{V,\rm DL}, \quad \text{(B.3)}$$

and identify the outlier QSOs that depart by more than $3\,\sigma$ from the expected linear relationship. Figure B.2 shows the typical QSO $E_{g,r}$ versus $A_{V,\rm DL}$ fit for $U_{\rm min} = 0.6$. In this case, $\eta_{g,r}(U_{\rm min} = 0.6) = 0.19$. Although the QSO $E_{X,Y}$ versus $A_{V,\rm DL}$ relationship has large scatter due to variations in the QSOs spectra (continuum and lines) and intrinsic obscuration in the QSOs, as long as there is no selection bias with respect to $A_{V,\rm DL}$ our study should be robust. The fact that the mean QSO $E_{X,Y}$ for each $A_{V,\rm DL}$ (curve) and the best fit of the QSO $E_{X,Y}$ versus $A_{V,\rm DL}$ (straight line) in Figure B.2 agree remarkably well, supports the validity of the preceding analysis.

Once we have computed $E_{X,Y}$ for all the band pairs and $U_{\rm min}$, we remove the QSOs that are considered as outliers in any of the computations to obtain a cleaner sample of "good" QSOs. We reiterate the full procedure twice using the "good" QSO sample

[22] See the discussion following Eq. B.6.

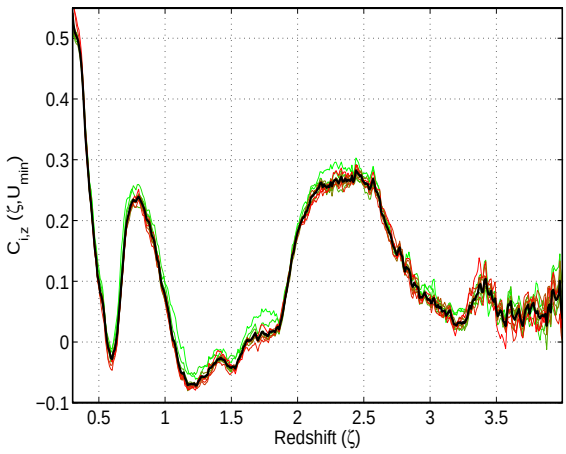

Fig. B.1. Unobscured QSO intrinsic colours, as a function of Redshift (ζ), for the bands i and z. The functions $C_{i,z}(\zeta, U_{\rm min})$, are shown for the different values of $U_{\rm min}$, using redder traces for larger $U_{\rm min}$, and greener for smaller $U_{\rm min}$. Their weighted mean $C_{i,z}(\zeta)$ is shown in black. The Lyα line affects the i band photometry for $\zeta > 4.62$, but we restrict our analysis to $\zeta < 3.35$ to have enough QSOs per Redshift interval. For $\zeta > 3.35$ the estimated $C_{i,z}(\zeta)$ becomes noisy.

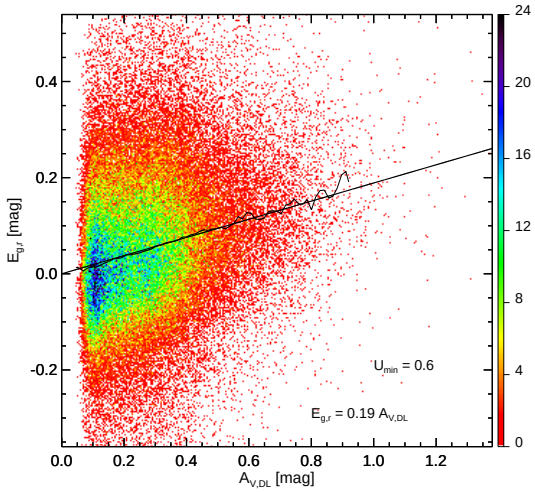

Fig. B.2. Colour excess $E_{g,r}$ versus $A_{V,\rm DL}$ for the QSOs with $U_{\rm min} = 0.6$. Colour corresponds to the density of points (see Figure 5). The straight line corresponds to the best fit for all the QSOs. For each $A_{V,\rm DL}$, the black curve correspond to the mean $E_{g,r}$ for the QSOs in an interval with radius $\delta A_{V,\rm DL} = 0.01$. Even though the QSOs show significant scatter, the $E_{g,r}$ versus $A_{V,\rm DL}$ relationship is very linear; the mean $E_{g,r}$ for each $A_{V,\rm DL}$ curve does not show significant departures from the straight line.

form the previous iteration, resulting in a final "cleanest" sample containing 224 245 QSOs with $\zeta < 3.35$ (for which we have Lyα free photometry in the r-, i-, and z-bands), 135,953 with $\zeta < 2.31$ (where we can use the r-band), and 77 633 QSO with $\zeta < 1.64$, where we can use all the SDSS bands. We have an estimate of the intrinsic colours $C_{X,Y}$, and an estimate of the reddening $E_{X,Y}$ for each QSO that is retained by the redshift constraints.

Even though the unobscured QSO intrinsic colours are computed independently for each band pair, we do obtain consistent results across the band pairs, i.e.,

$$C_{X,Y}(\zeta) - C_{Y,Z}(\zeta) \approx C_{X,Z}(\zeta), \tag{B.4}$$

holds for all the bands X, Y, and Z, over all the redshifts ζ considered. Working with the $\rm H_I$ column density maps as an estimate of the extinction instead of the $A_{V,\rm DL}$ gives very similar estimates of $C_{X-Y}(\zeta)$, and is independent of any dust modelling, so this means we did not translate potential dust modelling systematics into our QSO estimates.

In order to compare the $A_{V,\rm DL}$ estimate with a QSO estimate, we need to derive a QSO extinction A_V from the different colour excess $E_{X,Y}$. We proceed as follows.

For a given QSO spectrum and extinction curve shape, we can compute the SDSS magnitude increase per dust extinction A_X/A_V for $X = u$, g, r, i, and z. These ratios depend on the assumed extinction curve and QSO spectral shape, and therefore on the QSO redshift. Using the QSO composite spectrum of Vanden Berk et al. (2001) and the extinction curve presented by Fitzpatrick (1999) parametrized via R_V, we compute the ratios A_X/A_V:

$$\delta X(\zeta, R_V) \equiv A_X/A_V. \tag{B.5}$$

Figure B.3 shows $\delta X(\zeta, R_V = 3.1)$ as a function of the QSO redshift ζ, for the different bands $X = u$, g, r, i, and z. Even though the QSO intrinsic colours are strong functions of its redshift, the extinction curves are smooth enough that $\delta X(\zeta, R_V = 3.1)$ is mostly redshift independent.

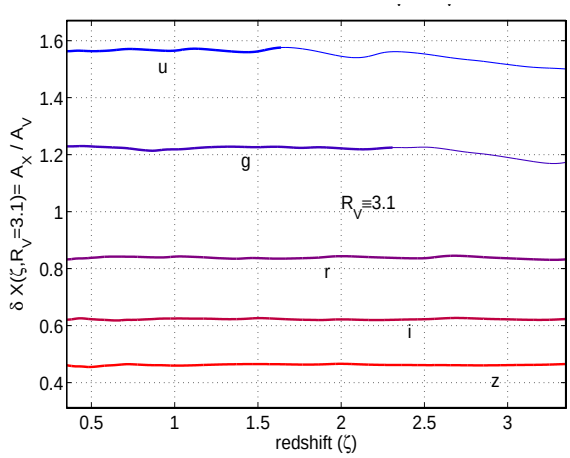

Fig. B.3. QSO magnitude increase per unit of dust extinction A_V as a function of the QSO redshift. We use an extinction curve with $R_V = 3.1$. The u and g band curves are shown in a thinner trace for $\zeta > 1.64$ and $\zeta > 2.31$, the redshifts at which the intergalactic Lyα line can affect the photometry in these bands.

Using the extinction curves with $R_V = 3.1$ (which was also used to constrain the optical properties of the grains used in the DL model), for each redshift ζ, we define:

$$\delta_{[X,Y]}(\zeta) = \frac{1}{\delta X(\zeta, R_V = 3.1) - \delta Y(\zeta, R_V = 3.1)}, \tag{B.6}$$

and

$$A_{V,\rm QSO,[X,Y]} = \delta_{[X,Y]} \times E_{X,Y}. \tag{B.7}$$

Finally, for each QSO, we define its $A_{V,\rm QSO}$ as the average of the $A_{V,\rm QSO,[X,Y]}$ values for all the band pairs that are allowed by its redshift ζ.

Appendix C: Impact of the CIB anisotropies and instrumental noise on the parameter estimation.

We study the impact of CIB anisotropies (CIBA) and instrumental (stochastic) noise in our mass estimates in the diffuse ISM

(where their effect should be the largest). We simulate data by adding CIBA and instrumental noise to DL SEDs, and fit them with the same technique as we use to fit the observed data. The results quantify the deviations of the recovered parameters from the original ones.

We start by a family of four DL SEDs with $U_{\rm min}$ = 0.4, 0.6, 0.8, and 1.0, a typical $f_{\rm PDR}$ = 0.05, and $q_{\rm PAH}$ = 0.03. We normalize each SED to the mean A_V found for the QSO lines of sight in each $U_{\rm min}$. We replicate each SED 100 000 times, add CIB anisotropies and instrumental noise. The noise added has 2 components. We add (band-to-band) independent noise to simulate stochastic instrumental noise with amplitudes given by *Pl*-MBB, Table B.1, 30′ resolution. We further add a typical CIB SED (also from *Pl*-MBB, Table B.1, 30′ row), that is completely correlated across the *Planck* bands, and partially correlated with the *IRAS* bands, as recommended in *Pl*-MBB, Appendix B. We finally fit each simulated SED with DL model, as we did in the main data fit.

Figure C.1 shows the recovered $\Sigma_{M_{\rm d}}$ divided by the original $\Sigma_{M_{\rm d}}$, and recovered $U_{\rm min}$ for the SEDs. Each set of points correspond to the different original $U_{\rm min}$. The inclined solid line correspond to the renormalization curve given by Eq. 9, (rescaled to match the mean A_V of the simulated SEDs). There is not a global bias in the recovered $\Sigma_{M_{\rm d}}$, nor $U_{\rm min}$; the distribution of the recovered $\Sigma_{M_{\rm d}}$ and $U_{\rm min}$ are centered in the original values. Although CIBA and instrumental noise do generate a trend in the same direction as the renormalization, their impact is significantly smaller than the observed renormalization: they do not span the full range found over the QSOs lines of sight. Moreover, the renormalization found in Section 6.3 is independent of the modelling resolution; one obtain similar renormalization coefficients working at 5′, 30′, and 60′ FWHM. For those resolutions, the instrumental noise and CIBA have a very different magnitude, and therefore, their impact would be quite different. Therefore, CIBA and instrumental noise are not a significant source of the A_V systematic departures with respect to $U_{\rm min}$ found in Section 6.3.

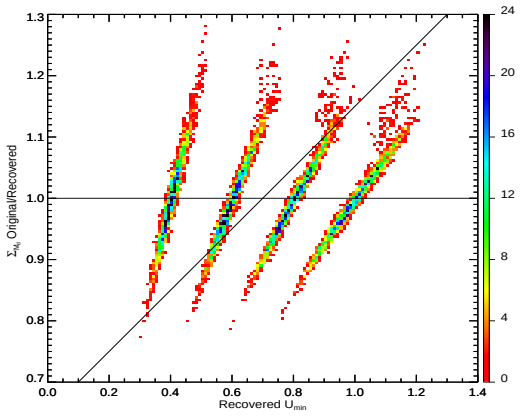

Fig. C.1. Comparison of the original and recovered dust mass under CIBA and instrumental noise simulation in the diffuse ISM. Colour corresponds to the density of points (see Figure 5).

[1] APC, AstroParticule et Cosmologie, Université Paris Diderot, CNRS/IN2P3, CEA/lrfu, Observatoire de Paris, Sorbonne Paris Cité, 10, rue Alice Domon et Léonie Duquet, 75205 Paris Cedex 13, France
[2] African Institute for Mathematical Sciences, 6-8 Melrose Road, Muizenberg, Cape Town, South Africa
[3] Agenzia Spaziale Italiana Science Data Center, Via del Politecnico snc, 00133, Roma, Italy
[4] Agenzia Spaziale Italiana, Viale Liegi 26, Roma, Italy
[5] Astrophysics Group, Cavendish Laboratory, University of Cambridge, J J Thomson Avenue, Cambridge CB3 0HE, U.K.
[6] Astrophysics & Cosmology Research Unit, School of Mathematics, Statistics & Computer Science, University of KwaZulu-Natal, Westville Campus, Private Bag X54001, Durban 4000, South Africa
[7] Atacama Large Millimeter/submillimeter Array, ALMA Santiago Central Offices, Alonso de Cordova 3107, Vitacura, Casilla 763 0355, Santiago, Chile
[8] CITA, University of Toronto, 60 St. George St., Toronto, ON M5S 3H8, Canada
[9] CNRS, IRAP, 9 Av. colonel Roche, BP 44346, F-31028 Toulouse cedex 4, France
[10] California Institute of Technology, Pasadena, California, U.S.A.
[11] Centro de Estudios de Física del Cosmos de Aragón (CEFCA), Plaza San Juan, 1, planta 2, E-44001, Teruel, Spain
[12] Computational Cosmology Center, Lawrence Berkeley National Laboratory, Berkeley, California, U.S.A.
[13] Consejo Superior de Investigaciones Científicas (CSIC), Madrid, Spain
[14] DSM/Irfu/SPP, CEA-Saclay, F-91191 Gif-sur-Yvette Cedex, France
[15] DTU Space, National Space Institute, Technical University of Denmark, Elektrovej 327, DK-2800 Kgs. Lyngby, Denmark
[16] Département de Physique Théorique, Université de Genève, 24, Quai E. Ansermet,1211 Genève 4, Switzerland
[17] Departamento de Física, Universidad de Oviedo, Avda. Calvo Sotelo s/n, Oviedo, Spain
[18] Department of Astrophysics/IMAPP, Radboud University Nijmegen, P.O. Box 9010, 6500 GL Nijmegen, The Netherlands
[19] Department of Physics & Astronomy, University of British Columbia, 6224 Agricultural Road, Vancouver, British Columbia, Canada
[20] Department of Physics and Astronomy, Dana and David Dornsife College of Letter, Arts and Sciences, University of Southern California, Los Angeles, CA 90089, U.S.A.
[21] Department of Physics and Astronomy, University College London, London WC1E 6BT, U.K.
[22] Department of Physics, Florida State University, Keen Physics Building, 77 Chieftan Way, Tallahassee, Florida, U.S.A.
[23] Department of Physics, Gustaf Hällströmin katu 2a, University of Helsinki, Helsinki, Finland
[24] Department of Physics, Princeton University, Princeton, New Jersey, U.S.A.
[25] Department of Physics, University of California, Santa Barbara, California, U.S.A.
[26] Department of Physics, University of Illinois at Urbana-Champaign, 1110 West Green Street, Urbana, Illinois, U.S.A.
[27] Dipartimento di Fisica e Astronomia G. Galilei, Università degli Studi di Padova, via Marzolo 8, 35131 Padova, Italy
[28] Dipartimento di Fisica e Scienze della Terra, Università di Ferrara, Via Saragat 1, 44122 Ferrara, Italy
[29] Dipartimento di Fisica, Università La Sapienza, P. le A. Moro 2, Roma, Italy
[30] Dipartimento di Fisica, Università degli Studi di Milano, Via Celoria, 16, Milano, Italy
[31] Dipartimento di Fisica, Università degli Studi di Trieste, via A. Valerio 2, Trieste, Italy
[32] Dipartimento di Fisica, Università di Roma Tor Vergata, Via della Ricerca Scientifica, 1, Roma, Italy
[33] Discovery Center, Niels Bohr Institute, Blegdamsvej 17, Copenhagen, Denmark
[34] Dpto. Astrofísica, Universidad de La Laguna (ULL), E-38206 La Laguna, Tenerife, Spain
[35] European Southern Observatory, ESO Vitacura, Alonso de Cordova 3107, Vitacura, Casilla 19001, Santiago, Chile

[36] European Space Agency, ESAC, Planck Science Office, Camino bajo del Castillo, s/n, Urbanización Villafranca del Castillo, Villanueva de la Cañada, Madrid, Spain
[37] European Space Agency, ESTEC, Keplerlaan 1, 2201 AZ Noordwijk, The Netherlands
[38] Facoltà di Ingegneria, Università degli Studi e-Campus, Via Isimbardi 10, Novedrate (CO), 22060, Italy
[39] HGSFP and University of Heidelberg, Theoretical Physics Department, Philosophenweg 16, 69120, Heidelberg, Germany
[40] Helsinki Institute of Physics, Gustaf Hällströmin katu 2, University of Helsinki, Helsinki, Finland
[41] INAF - Osservatorio Astrofisico di Catania, Via S. Sofia 78, Catania, Italy
[42] INAF - Osservatorio Astronomico di Padova, Vicolo dell'Osservatorio 5, Padova, Italy
[43] INAF - Osservatorio Astronomico di Roma, via di Frascati 33, Monte Porzio Catone, Italy
[44] INAF - Osservatorio Astronomico di Trieste, Via G.B. Tiepolo 11, Trieste, Italy
[45] INAF/IASF Bologna, Via Gobetti 101, Bologna, Italy
[46] INAF/IASF Milano, Via E. Bassini 15, Milano, Italy
[47] INFN, Sezione di Bologna, Via Irnerio 46, I-40126, Bologna, Italy
[48] INFN, Sezione di Roma 1, Università di Roma Sapienza, Piazzale Aldo Moro 2, 00185, Roma, Italy
[49] INFN/National Institute for Nuclear Physics, Via Valerio 2, I-34127 Trieste, Italy
[50] IPAG: Institut de Planétologie et d'Astrophysique de Grenoble, Université Grenoble Alpes, IPAG, F-38000 Grenoble, France, CNRS, IPAG, F-38000 Grenoble, France
[51] Imperial College London, Astrophysics group, Blackett Laboratory, Prince Consort Road, London, SW7 2AZ, U.K.
[52] Infrared Processing and Analysis Center, California Institute of Technology, Pasadena, CA 91125, U.S.A.
[53] Institut Universitaire de France, 103, bd Saint-Michel, 75005, Paris, France
[54] Institut d'Astrophysique Spatiale, CNRS (UMR8617) Université Paris-Sud 11, Bâtiment 121, Orsay, France
[55] Institut d'Astrophysique de Paris, CNRS (UMR7095), 98 bis Boulevard Arago, F-75014, Paris, France
[56] Institute for Space Sciences, Bucharest-Magurale, Romania
[57] Institute of Astronomy, University of Cambridge, Madingley Road, Cambridge CB3 0HA, U.K.
[58] Institute of Theoretical Astrophysics, University of Oslo, Blindern, Oslo, Norway
[59] Instituto de Astrofísica de Canarias, C/Vía Láctea s/n, La Laguna, Tenerife, Spain
[60] Instituto de Física de Cantabria (CSIC-Universidad de Cantabria), Avda. de los Castros s/n, Santander, Spain
[61] Jet Propulsion Laboratory, California Institute of Technology, 4800 Oak Grove Drive, Pasadena, California, U.S.A.
[62] Jodrell Bank Centre for Astrophysics, Alan Turing Building, School of Physics and Astronomy, The University of Manchester, Oxford Road, Manchester, M13 9PL, U.K.
[63] Kavli Institute for Cosmology Cambridge, Madingley Road, Cambridge, CB3 0HA, U.K.
[64] LAL, Université Paris-Sud, CNRS/IN2P3, Orsay, France
[65] LERMA, CNRS, Observatoire de Paris, 61 Avenue de l'Observatoire, Paris, France
[66] Laboratoire AIM, IRFU/Service d'Astrophysique - CEA/DSM - CNRS - Université Paris Diderot, Bât. 709, CEA-Saclay, F-91191 Gif-sur-Yvette Cedex, France
[67] Laboratoire Traitement et Communication de l'Information, CNRS (UMR 5141) and Télécom ParisTech, 46 rue Barrault F-75634 Paris Cedex 13, France
[68] Laboratoire de Physique Subatomique et de Cosmologie, Université Joseph Fourier Grenoble I, CNRS/IN2P3, Institut National Polytechnique de Grenoble, 53 rue des Martyrs, 38026 Grenoble cedex, France
[69] Laboratoire de Physique Théorique, Université Paris-Sud 11 & CNRS, Bâtiment 210, 91405 Orsay, France
[70] Lawrence Berkeley National Laboratory, Berkeley, California, U.S.A.
[71] Max-Planck-Institut für Astrophysik, Karl-Schwarzschild-Str. 1, 85741 Garching, Germany
[72] McGill Physics, Ernest Rutherford Physics Building, McGill University, 3600 rue University, Montréal, QC, H3A 2T8, Canada
[73] National University of Ireland, Department of Experimental Physics, Maynooth, Co. Kildare, Ireland
[74] Niels Bohr Institute, Blegdamsvej 17, Copenhagen, Denmark
[75] Observational Cosmology, Mail Stop 367-17, California Institute of Technology, Pasadena, CA, 91125, U.S.A.
[76] Princeton University Observatory, Peyton Hall, Princeton, NJ 08544-1001, U.S.A.
[77] SISSA, Astrophysics Sector, via Bonomea 265, 34136, Trieste, Italy
[78] School of Physics and Astronomy, Cardiff University, Queens Buildings, The Parade, Cardiff, CF24 3AA, U.K.
[79] Space Research Institute (IKI), Russian Academy of Sciences, Profsoyuznaya Str, 84/32, Moscow, 117997, Russia
[80] Space Sciences Laboratory, University of California, Berkeley, California, U.S.A.
[81] Special Astrophysical Observatory, Russian Academy of Sciences, Nizhnij Arkhyz, Zelenchukskiy region, Karachai-Cherkessian Republic, 369167, Russia
[82] Sub-Department of Astrophysics, University of Oxford, Keble Road, Oxford OX1 3RH, U.K.
[83] UPMC Univ Paris 06, UMR7095, 98 bis Boulevard Arago, F-75014, Paris, France
[84] Université de Toulouse, UPS-OMP, IRAP, F-31028 Toulouse cedex 4, France
[85] Universities Space Research Association, Stratospheric Observatory for Infrared Astronomy, MS 232-11, Moffett Field, CA 94035, U.S.A.
[86] University of Granada, Departamento de Física Teórica y del Cosmos, Facultad de Ciencias, Granada, Spain
[87] University of Granada, Instituto Carlos I de Física Teórica y Computacional, Granada, Spain
[88] Warsaw University Observatory, Aleje Ujazdowskie 4, 00-478 Warszawa, Poland